Avoiding Ionic Interference in Computing the Ideality Factor for Perovskite Solar Cells and an Analytical Theory of Their Impedance-Spectroscopy Response

Laurence J. Bennett,[1] Antonio J. Riquelme,[2] Juan A. Anta,[2] Nicola E. Courtier,[3] and
Giles Richardson[1,*]

[1]*Mathematical Sciences, University of Southampton, Southampton SO17 1BJ, United Kingdom*

[2]*Área de Química Física, Universidad Pablo de Olavide, Seville E-41013, Spain*

[3]*Department of Engineering Science, University of Oxford, Oxford OX1 3PJ, United Kingdom*

Impedance spectroscopy (IS) is a straightforward experimental technique that is commonly used to obtain information about the physical and chemical characteristics of photovoltaic devices. However, the nonstandard physical behavior of perovskite solar cells (PSCs), which are heavily influenced by the motion of mobile ion vacancies, has hindered efforts to obtain a consistent theory of PSC impedance. This work rectifies this omission by deriving a simple analytic model of the impedance response of a PSC from the underlying drift-diffusion model of charge-carrier dynamics and ion-vacancy motion, via an intermediate model that shows extremely good agreement with the drift-diffusion model in the relevant parameter regimes. Excellent agreement is demonstrated between the analytic impedance model and the much more complex drift-diffusion model for applied biases (including both open circuit and the maximum power point at 0.1 and 1 Sun) close to the cell's built-in voltage V_{bi}. Both models show good qualitative agreement to experimental IS data in the literature and predict many of the observed anomalous features found in impedance measurements on PSCs. The analytic model provides a practical and useful tool with which to interpret PSC impedance data and extract physical parameters from IS experiments. We define a physical parameter, n_{el} (the electronic ideality factor), that is of particular significance to PSC physics, since, in contrast to the apparent ideality factor, the value of n_{el} can be used to identify the dominant source of recombination in the cell independent of its ionic properties.

I. INTRODUCTION

Over the last decade, metal halide perovskite solar cells (PSCs) have emerged as a promising photovoltaic technology. Certified power conversion efficiencies of 25.5% and 29.5% have been obtained for single junction and tandem PSC configurations, respectively [1–3]. The high efficiencies of perovskite solar cells are competitive with established technologies; however, concerns over their long-term stability and an incomplete description of their fundamental physics, present barriers to widespread commercialization [4–6].

Impedance spectroscopy (IS) is a characterization method that probes the physical and chemical properties of (photo)electrochemical devices under operation [7,8]. Measurement of impedance involves applying a dc voltage V_{dc} with an additional small sinusoidal voltage perturbation, of frequency ω, to the system and measuring the current response. The applied voltage for an impedance

measurement takes the form

$$V(t) = V_{dc} + V_p \cos(\omega t). \tag{1}$$

By design, the amplitude V_p is small enough to ensure that the current response is linearly dependent on the voltage input. Although the resulting current response varies sinusoidally with the same frequency as the voltage input, its magnitude and phase lag depend on the frequency ω and the dc voltage. The relationship between current response and the input voltage is frequently represented in the form of a complex impedance $Z(\omega)$, such that

$$Z(\omega) = |Z(\omega)|e^{-i\theta(\omega)}, \tag{2}$$

where the magnitude, $|Z(\omega)| = V_p/J_p(\omega)$ and the phase, $\theta(\omega)$ are obtained from the current response, which takes the form

$$J(t) = J_{dc} + J_p(\omega) \cos(\omega t + \theta(\omega)). \tag{3}$$

Here, J_{dc} is the steady-state component and J_p is the amplitude of the sinusoidal component of the current response.

*g.richardson@soton.ac.uk

The impedance is often expressed in terms of its real and imaginary components

$$\mathrm{Re}(Z(\omega)) = \mathrm{R}(\omega), \quad \mathrm{Im}(Z(\omega)) = \mathrm{X}(\omega). \quad (4)$$

Here R is termed the resistance and X the reactance. Impedance spectra are determined, at fixed dc voltage V_{dc}, by measuring the cell's response to small voltage perturbations over a range of frequencies ω. Further information about the cell's properties can be obtained by collecting impedance spectra at different dc voltages, illumination intensities, and temperatures.

Impedance spectroscopy measurements are relatively simple to perform and require equipment that is commonly found in labs. With the correct interpretation, IS has the potential to offer significant insight into the physics and characteristics of PSCs. In addition to allowing the interrogation of the recombination pathways [9], it allows ionic properties and interfacial potentials [9,10] to be probed, both of which have been proposed as factors that strongly influence chemical reactivity and degradation [11–13]. One of the main advantages of IS over other characterization techniques is that it can be performed on complete devices under working conditions. In contrast, many other characterization techniques are performed on half cells, or rely on destructive methods [14–16]. The fact that IS is cheap and convenient has resulted in its widespread use in the field of PSCs, despite the current absence of a firm theoretical basis with which to interpret the measurements. The nondestructive nature of IS has led to it being used to monitor device stability over time [10,17], which, when paired with the accurate interpretation techniques for IS described here, opens the prospect of an inexpensive tool with which to understand the causes of degradation.

The spectrum of a PSC typically exhibits two (or more) time constants that result in semicircular features on a Nyquist diagram [a plot of $-\mathrm{Im}(Z(\omega))$ versus $\mathrm{Re}(Z(\omega))$]. A low-frequency (LF) feature is observed at around 10^{-2}–10^1 Hz and a high-frequency (HF) feature is seen around 10^4–10^6 Hz [18–20]. Less significant intermediate frequency features, such as loops or "bumps" are sometimes seen that correspond to additional time constants [18,21–24]. The presence and magnitude of these features varies significantly between cells of different compositions and under different experimental conditions. Figure 1(a) illustrates a typical Nyquist plot for a PSC while Figs. 1(b) and 1(d) show the corresponding frequency plots. The phenomenological "*RC-RC*" equivalent circuit, which is commonly employed to extract resistances and capacitances from PSC impedance spectra, is shown in Fig. 1(c).

The main difficulty in extracting useful physical information from IS measurements conducted on PSCs is that the physics of these cells is, to a large extent, determined by the motion of large numbers of slow-moving ion vacancies and so is markedly different to that of other photovoltaic devices. Intuition brought to the perovskite field by experts in IS, who previously worked on other types of device, is therefore often useless because it is confounded by the unusual physics of these perovskite devices. Useful interpretation of IS results should therefore be based on a PSC model that captures the effects of ion motion. IS results for PSCs are commonly fitted to equivalent circuit models in an attempt to extract useful information from the spectra, but this approach can only yield sensible conclusions if all the elements in the equivalent circuit can be related to real physical processes occurring in the device. For instance, the resistances and capacitances extracted from the ad hoc "*RC-RC*" equivalent circuit are hard to interpret, as illustrated by predictions of *negative* capacitances obtained by fitting this circuit to data obtained from some cells. In this context we note four recent works that have compared results from IS experiments to drift-diffusion simulations, which incorporate the effects
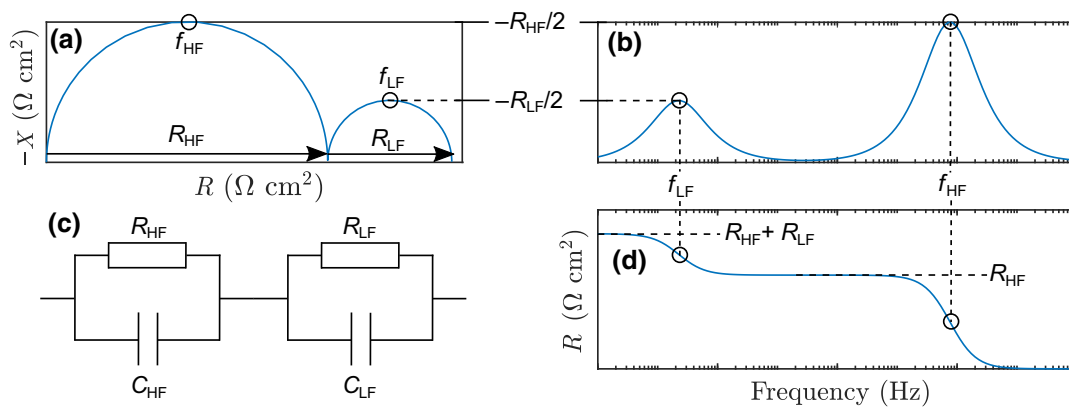

FIG. 1. (a) Nyquist, (b),(d) frequency plots with key impedance parameters labeled for a typical PSC impedance spectra exhibiting two features. (c) An *RC-RC* equivalent circuit used to extract resistances and capacitances. The labeled frequencies are related to the angular frequencies via $f = \omega/2\pi$. The low-frequency semicircle can lie below the axis on the Nyquist plot, resulting in negative LF resistance and capacitance values (see, for example, Refs. [25,26]).

of ion-vacancy motion, namely [9,27–29]. These works all require that the IS response is simulated computationally from a drift-diffusion model of the device that incorporates the motion of both ions and charge carriers. Such models are based on a large set of device parameters that must be specified before the numerical results can be compared to the experimental ones. This leads to a costly fitting process in which the device parameters are repeatedly adjusted, and the simulations rerun, until the simulated IS results mimic the experimental ones. Nevertheless, drift-diffusion models have the advantage that all parameters (diffusion coefficients, carrier concentrations, lifetimes, etc.) have a clear physical meaning. The aim of this work is to avoid this cumbersome fitting process by seeking approximate (yet highly accurate) analytic solutions to the drift-diffusion model that can be directly compared to the experimental IS results, and thereby used to extract device parameters from experimental data without the need for large numbers of computational simulations.

Moia and coworkers [27] report analytical expressions that describe the impedance response of the perovskite solar cell, such as the recombination resistance. However, in order to do this, they employ an ad hoc approach in which they compare results from an equivalent circuit (based on a "bipolar *n-p-n*" transistor) to numerical results from a drift-diffusion model. Good agreement is only obtained after modifying the equivalent circuit model by defining an ionic resistance and capacitance. In contrast, our analytical expressions are directly derived from the drift-diffusion equations themselves, by introducing suitable approximations, leading to a description of the impedance response that is closely related to an *RC-RC* equivalent circuit.

Determination of a solar cell's ideality factor is one of the simplest and therefore most popular methods to identify the source of recombination loss [30]. Various authors have attempted to relate the value of the ideality factor to the recombination processes occurring within a PSC [31–34]. However, a comprehensive framework for interpreting ideality factor measurements for PSCs has yet to be established. This is primarily because of a reliance on classical semiconductor theory, which is not directly applicable to devices (such as perovskite cells), which contain large numbers of mobile ions. Hence, it is perhaps not surprising that for PSCs recombination cannot be directly inferred from the ideality factor determined using the standard measurement techniques. These techniques, such as illumination versus open-circuit (Suns-V_{OC}) or dark J-V methods, lead to predictions of an "apparent" ideality factor that is voltage dependent, highly sensitive to ion concentration (see, for example, Ref. [9]) and has a value that spans a range less than 0.9 to greater than 5 [34–37]. Evidently, this is not concordant with interpretations formed from a naive analysis of recombination based on the Shockley diode equation. As is pointed out in Ref. [38],

this is hardly surprising since the physics of no other common photovoltaic is as strongly influenced by ion vacancies as is that of PSCs. Instead, in Ref. [38], it is suggested that the ideality factor obtained via the standard techniques should instead be interpreted as an "ectypal factor", and which is here termed the "apparent ideality factor."

The analytic approach we adopt here leads directly to an additional factor to the apparent ideality factor, which we label the electronic ideality factor n_{el}, that is independent of the parameters governing ion motion and close to being constant over a wide range of applied voltages. Moreover, it serves as an analog to the ideality factor that is typically used for conventional photovoltaic devices and can be used to identify the dominant recombination mechanism in a PSC. In particular, the value of n_{el} can distinguish between recombination occurring at the interfaces with the transport layers and in the perovskite. This is potentially a powerful diagnostic tool, because IS is a much quicker and cheaper technique to apply to the problem of determining the location of the dominant recombination losses than performing photoluminescence on the component structures of the cell, see, for example, Refs. [16,39,40]. Furthermore, as is pointed out in Ref. [16], most modern efficient cells are sufficiently well engineered so that little recombination occurs in the perovskite absorber layer compared to on the perovskite interfaces. Using IS, on working devices, to obtain n_{el} thus provides a relatively cheap way to assess the state of health of the perovskite absorber layer and, in particular, to determine whether the perovskite has so deteriorated as to become the primary focus of recombination losses.

To summarize our approach, in Sec. II we employ a coupled electronic-ionic drift-diffusion model [detailed in Eqs. (1)–(15) of Ref. [41]] to describe the operational physics of a planar PSC. A systematic, and highly accurate, approximation of this drift-diffusion model [41,42], termed the surface polarization model, is used to reduce the complexity of the drift-diffusion equations. This approximate model is able to accurately describe the evolution of the mobile ion vacancies and the electric potential and so can be used to predict the results of impedance measurements. We show further that in scenarios in which the electron and hole distributions are close to being Boltzmann distributed our impedance model can be reduced to a tractable set of analytic expressions for the key properties (i.e., a set of transcendental equations). Assuming a Boltzmann distribution for the charge carriers turns out (as we show) to be a good approximation to the real behavior in regimes where impedance experiments are most commonly conducted, i.e., where the applied voltage lies in the vicinity of the open-circuit voltage and the maximum power point. This approach yields analytic impedance formulae for the low- and high-frequency resistances and capacitances, which are given in Sec. III. In Sec. IV direct, and favorable, comparison is made between Nyquist (and

frequency) plots obtained from these impedance formulae and from numerical solutions to the full drift-diffusion model (see, for example, Figs. 4, 6, and 12). In Sec. V we define the electronic ideality factor and demonstrate, by comparison with numerical solution of the drift diffusion model, how it can be used to determine the location and nature of the dominant type of charge-carrier recombination occurring within the cell. In Sec. VI we use the analytic model that we develop to discuss how commonly observed impedance features can be interpreted in terms of a cell's physical properties before briefly touching upon an extension to the theory to scenarios in which more than one recombination mechanism has a significant effect on the cell's behavior. Finally, in Sec. VII we draw our conclusions.

From a pragmatic perspective our results provide a practical tool with which to interpret, and to extract useful information from, experimental impedance spectra of perovskite solar cells and other related devices with substantial ionic motion.

II. ANALYTIC MODEL DERIVATION

To derive an analytic model for the impedance response of a PSC, we start from the standard coupled drift-diffusion model [as formulated in Eqs. (1)–(15) of Ref. [41]] for charge-carrier transport across the cell and the motion of a single ion species in the perovskite absorber (see also Refs. [27,29,43–46]). Drift-diffusion models of this type have been shown to be capable of reproducing the impedance spectra of PSCs [9,27–29]. Here we do not explicitly write down the coupled drift-diffusion model given in Ref. [41] but, with only two exceptions, our notation coincides exactly with that in this work so that the parameters given in Table I can be used directly in simulations of the drift-diffusion Eqs. (1)–(15). The exceptions to this are that, in Ref. [41], the work functions in the transport layers [W_E and W_H, in the electron transport layer (ETL) and hole transport layer (HTL), respectively] are defined directly, [47] whereas in this work these quantities are related to the band edges, density of states, and effective doping densities in these materials via the relations

$$W_E = -E_{CE} + k_B T \log_e \left(\frac{g_{CE}}{d_E} \right), \qquad (5)$$

$$W_H = -E_{VH} - k_B T \log_e \left(\frac{g_{VH}}{d_H} \right). \qquad (6)$$

Assuming that there is no significant potential drop on the outer edges of the transport layers and that they are sufficiently strongly doped, these relations can also be used to compute the cell's built-in voltage V_{bi} from the standard

TABLE I. Parameter definitions and their values used in this work.

	Description	Value	Refs.
Constants			
q	Elementary charge	1.60×10^{-19} C	
ε_0	Permittivity of free space	8.85×10^{-12} Fm^{-1}	
MAPbI$_3$ properties			
b	Width	300 nm	[56,57]
α	Absorption coefficient	1.3×10^7 m^{-1}	[58]
ε_p	Permittivity	$24.1\varepsilon_0$	[59]
E_C	Conduction-band minimum	-3.8 eV	[60]
E_V	Valence-band maximum	-5.4 eV	[60]
g_C	Conduction-band DOS	8.1×10^{24} m^{-3}	[59]
g_V	Valence-band DOS	5.8×10^{24} m^{-3}	[59]
D_n	Electron diffusion coeff.	1.7×10^{-4} m^2 s^{-1}	[61]
D_p	Hole diffusion coeff.	1.7×10^{-4} m^2 s^{-1}	[61]
D_+	Ion-vacancy diffusion coeff.	1×10^{-16} m^2 s^{-1}	[46,48]
N_0	Ion-vacancy density	1.6×10^{25} m^{-3}	[62]
ETL properties (compact TiO$_2$)			
b_E	Width	100 nm	
d_E	Effective doping density	5×10^{24} m^{-3}	
ε_E	Permittivity	$10\varepsilon_0$	
D_E	Electron diffusion coeff.	1×10^{-5} m^2 s^{-1}	
g_{CE}	Eff. conduction-band DOS	1×10^{26} m^{-3}	
E_{CE}	Conduction-band minimum	-4.1 eV	[63]
HTL properties (Spiro)			
b_H	Width	200 nm	
d_H	Effective doping density	5×10^{24} m^{-3}	
ε_H	Permittivity	$3\varepsilon_0$	
D_H	Hole diffusion coefficient	1×10^{-6} m^2 s^{-1}	
g_{VH}	Eff. valence-band DOS	1×10^{26} m^{-3}	
E_{VH}	Valence-band maximum	-5.1 eV	[60]
Other			
T	Temperature	298 K	
V_T	Thermal voltage (298 K)	25.7 mV	
F_{ph}	Incident photon flux	1.4×10^{21} m^{-2} s^{-1}	
V_{bi}	Built-in voltage	0.85 V	

formula

$$V_{bi} = \frac{1}{q}(W_H - W_E). \qquad (7)$$

Unlike other photovoltaics the response of PSCs is determined not only by the motion of the charge carriers (electrons and holes) but also by that of mobile ion vacancies. This makes their physics more complex than that of other solar cells. As has been noted by Eames *et al.* [48] ion vacancies occur at much higher densities than those of the charge carriers, and furthermore move much more slowly than the charge carriers. Since the perovskite is a crystal made of at least three ionic species, for example MAPbI$_3$ is made of methylammonium ions (CH$_3$NH$_3^+$), iodide ions (I$^-$) and lead ions (Pb^{2+}), multiple species of vacancy may play a role in

the cell's response. In the case of MAPbI$_3$ it is known, both from experiment [49,50] and from *ab initio* molecular calculations [48], that there is significant motion of the relatively mobile iodide ion vacancies and, it is suspected, that the much less mobile methylammonium ion vacancies may also influence the physics over much longer timescales, of the order of several hours [51]. The comparatively large density of mobile charged ion vacancies in the perovskite crystal structure means that the internal electric field within the device is, to a very good approximation, determined almost solely by the ion-vacancy distributions, and is almost completely unaffected by those of the charge carriers [42]. In addition, mobile ion vacancies are believed to occur at sufficiently high densities to result in the formation of narrow space-charge (or Debye) layers at the interfaces between the perovskite and the transport layers (see, for example, Refs. [15,48]). Indeed it seems that a space-charge layer is a requirement for simulations to reproduce the experimental behaviors characteristic of the impedance of PSCs [27–29,41,45,46].

The question of whether the perovskite is either doped or intrinsic is the subject of controversy. It seems that this depends strongly on the substrate, the particular perovskite formulation and the preparation conditions [52–54]. For example, Weber *et al.* [15] use Kelvin probe force microscopy measurements to show (see Fig. 4) that there are significant electric fields within the perovskite layer, which evolve only over a relatively long timescale (around 0.5 s). This would not be possible if the perovskite was heavily doped. Therefore, for the purposes of this model, it is assumed that the level of doping within the perovskite is low enough that it is appropriate to approximate it as intrinsic.

The total potential drop across the cell $V_{bi} - V(t)$ is composed of a built-in potential V_{bi}, arising from differences in the Fermi levels of the two transport layers adjacent to the perovskite, and the applied voltage $V(t)$, as shown in Fig. 2. It is usually a reasonable assumption that the energy levels of the transport layers and their contacts line up, so that there is no significant potential drop at the outer edges of the ETL and the HTL, and furthermore, that there is some level of doping within the transport layers so that the internal electric field in the transport layers is minimal. Then, as shown in Ref. [41], the total potential drop across the cell occurs predominantly within the perovskite layer, in the form of a uniform electric field $E(t)$, and across the two space-charge layers that form at the interfaces between the perovskite and the ETL and between the perovskite and the HTL. The recombination losses within the cell, and therefore its behavior, depends sensitively on how the total potential drop $V_{bi} - V(t)$ is distributed across the cell [38]. This motivates the subdivision of the potential drop $V_{bi} - V(t)$ into five component drops V_1, V_2, $bE(t)$, V_3, and V_4 occurring
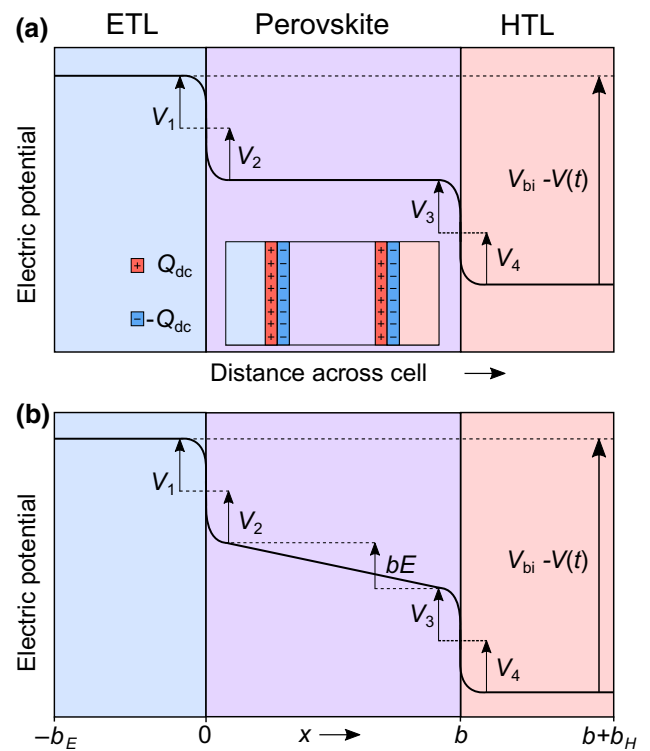

FIG. 2. (a) Diagram illustrating the potential drops V_1-V_4 across a perovskite solar cell at steady state. Inset shows the charge contained within the perovskite space-charge layers at steady state. (b) Diagram illustrating the potential across a PSC with a nonzero uniform bulk electric field after a rapid reduction to the applied voltage.

across the different regions of the cell, as illustrated in Fig. 2(b).

A. The surface polarization model (or ionic capacitance model)

1. Capacitance relations and internal electric field.

For both the steady-state and non-steady-state configurations capacitance relations may be determined from the underlying drift-diffusion model of the device. This gives V_{1-4} in terms of the charge Q (per unit area) contained in the space-charge layers. The exact functional forms of $V_1(Q)$, $V_2(Q)$, $V_3(Q)$, and $V_4(Q)$ are contingent on the physics of the device. In the widely considered scenario where there is a single mobile positively charged ion species (typically a halide vacancy) confined to the perovskite layer, and where both electron and hole transport layers are moderately doped, these capacitance relations have been derived in Refs. [41,42] from the corresponding, and extensively used, version of the drift-diffusion model [27,29,41,43–46]. In deriving the surface polarization model, it is found that the space charge Q due to the accumulation of ions in the right perovskite space-charge layer is balanced by an equal and opposite space charge

$(-Q)$ in the left perovskite space-charge layer. [41,42]. Since, in Sec. III, we compare our approximate expressions for the high- and low-frequency resistances and capacitances against those obtained from impedance spectra generated by this version of the drift-diffusion model, we restate these capacitance relations below

$$
\begin{aligned}
V_1(Q) &= -\mathcal{V}(-\Omega_E Q), & V_2(Q) &= -\mathcal{V}(-Q), \\
V_3(Q) &= \mathcal{V}(Q), & V_4(Q) &= -\mathcal{V}(-\Omega_H Q),
\end{aligned}
\tag{8}
$$

where

$$
\Omega_E = \sqrt{\frac{\varepsilon_p N_0}{\varepsilon_E d_E}}, \quad \Omega_H = \sqrt{\frac{\varepsilon_p N_0}{\varepsilon_H d_H}},
\tag{9}
$$

and $\mathcal{V}(Q)$ is the inverse of the function

$$
Q(\mathcal{V}) = \sqrt{q N_0 \varepsilon_p V_T} \, \mathrm{sign}(\mathcal{V}) \sqrt{2} \left(e^{\mathcal{V}/V_T} - \mathcal{V}/V_T - 1 \right)^{\frac{1}{2}},
\tag{10}
$$

where ε_p is the perovskite permittivity, N_0 is the mean ionic vacancy density, q is the elementary charge, and V_T is the thermal voltage (equal to $k_B T/q \approx 26$ mV). The parameters ε_E, ε_H, d_E, d_H and all material parameters that appear in these equations and those that follow are defined in Table I. Although the version of the capacitance model described above in Eqs. (8)–(10) applies only to the specific drift-diffusion model discussed above (and stated in full in Ref. [41]), it will often be possible to derive analogous capacitance relations for other versions of the drift-diffusion model, which describe a modified physical picture of a PSC (for example, one in which both anion and cation vacancies are mobile, or one in which the charge carriers in the transport layers obey degenerate statistics).

2. Evolution of the space charge

Under non-steady-state conditions, the space charge $Q(t)$ (per unit area) evolves in response to the motion of ion vacancies driven across the perovskite by the internal uniform electric field and, in the case of a single positively charged ion-vacancy species [46], evolves according to the ordinary differential equation (ODE)

$$
\frac{dQ}{dt} = \frac{q D_+ N_0}{V_T} E(t),
\tag{11}
$$

in which D_+ is the vacancy diffusivity. Here (as in Refs.[27]–[29]), it is assumed that positively charged mobile anion vacancies in the perovskite are balanced by a uniform distribution of negatively charged cation vacancies, with density N_0. This ensures that there is no net ionic charge in the layer. Since the ion motion is relatively slow, the charge within the space-charge layers lags behind the changes in the applied voltage leading to a non-negligible

internal uniform electric field that is determined by the relation

$$
E(t) = \frac{1}{b} \Big[V_{\mathrm{bi}} - V(t) - \Big(V_1(Q) + V_2(Q) + V_3(Q) + V_4(Q) \Big) \Big],
\tag{12}
$$

where the space charge is a function of time, i.e., $Q = Q(t)$.

3. Evolution of internal potential during IS experiment

In order to investigate the impedance response of the cell we first consider its steady-state behavior subjected to the constant applied voltage V_{dc}. In this configuration, we denote the excess charge (per unit area) contained within the left- and right-hand space-charge layers, lying within the perovskite, as $-Q_{\mathrm{dc}}$ and $+Q_{\mathrm{dc}}$ respectively [see Fig. 2(a)]. At steady-state the bulk electric field within the central portion of the perovskite is zero such that the charge density within the space charge layers is found, on appealing to (12), to satisfy the transcendental equation

$$
V_1(Q_{\mathrm{dc}}) + V_2(Q_{\mathrm{dc}}) + V_3(Q_{\mathrm{dc}}) + V_4(Q_{\mathrm{dc}}) = V_{\mathrm{bi}} - V_{\mathrm{dc}},
\tag{13}
$$

from which it is possible to determine Q_{dc} from the applied voltage V_{dc}. For the capacitance model described here it is not possible to determine an analytic solution for the steady-state ionic surface charge density Q_{dc} in terms of V_{dc}. Therefore, a numerical root finding algorithm is used to determine Q_{dc} for a given applied potential V_{dc}. Specifically, the built-in MATLAB root finder fzero [55] is used to obtain the solution to the nonlinear Eq. (13). This is the only part of the solution that requires numerical evaluation, the rest is analytic. Henceforth, non-steady-state conditions are denoted as functions of time [e.g., $Q(t)$], while steady-state conditions are expressed as functions of Q_{dc}. The response of the internal electric field of the cell to the impedance input voltage (1) can be readily calculated from the simplified capacitance model simply by substituting Eq. (1) into Eqs. (11)–(12), which on solution of the first-order ODE leads to a complete time course for the quantities $V_1(Q(t))$-$V_4(Q(t))$ and $E(t)$.

B. Approximate carrier distributions

On solution to the ionic model (8)–(13), the charge-carrier concentrations, and hence also the recombination losses and the current, can be found by solving a *linear* drift-diffusion model for the charge carriers, as described in Sec. B within the Supplemental Material of Ref. [41]. However, in order to arrive at a tractable analytic result, from which the influence of the parameters within the model on the impedance response of the cell can be readily inferred, we make the additional assumption (also used

in Ref. [38]), which is appropriate when the cell is held at an applied voltage in the vicinity of V_{OC}, that the charge carriers (holes and electrons) lie in approximate quasiequilibrium with the electric potential, i.e., that they are Boltzmann distributed.

Recombination at the interfaces between the perovskite and the transport layers is known to be a significant source of energy loss within the cell and, in order to account for this, we need not only to compute the electron and hole densities $n(x,t)$ and $p(x,t)$ within the central bulk region of the perovskite, but also at the interfaces between the perovskite and transport layers. At the ETL/perovskite interface (on $x = 0$) we denote the electron density within the ETL by $n_{ETL}^{(l)}$ and the hole density within the perovskite by $p^{(l)}$. Correspondingly, at the perovskite/HTL interface ($x = b$) we denote the electron density within the perovskite by $n^{(r)}$ and the hole density within the HTL by $p_{HTL}^{(r)}$. On assuming the carriers are Boltzmann distributed, the expressions for electron and hole densities within the perovskite layer, $0 < x < b$, read as follows:

$$n(x,t) = k_E d_E \exp\left(-\frac{V_1 + V_2 + xE}{V_T}\right),$$
$$p(x,t) = k_H d_H \exp\left(-\frac{V_3 + V_4 + (b-x)E}{V_T}\right),$$
(14)

on $x = 0$ the ETL/perovskite interface

$$n_{ETL}^{(l)}(t) = d_E \exp\left(-\frac{V_1}{V_T}\right),$$
$$p^{(l)}(t) = k_H d_H \exp\left(-\frac{V_2 + V_3 + V_4 + bE}{V_T}\right),$$
(15)

and on $x = b$ the perovskite/HTL interface

$$n^{(r)}(t) = k_E d_E \exp\left(-\frac{V_1 + V_2 + V_3 + bE}{V_T}\right),$$
$$p_{HTL}^{(r)}(t) = d_H \exp\left(-\frac{V_4}{V_T}\right).$$
(16)

Here, k_E and k_H are the ratios between the electron and hole densities across the ETL/perovskite and perovskite/HTL boundaries, respectively, and are given by

$$k_E = \frac{g_C}{g_{CE}} \exp\left(\frac{E_{CE} - E_C}{V_T}\right),$$
$$k_H = \frac{g_V}{g_{VH}} \exp\left(\frac{E_V - E_{VH}}{V_T}\right),$$
(17)

in which the parameters appearing in this equation are defined in Table I. Note that the discontinuity in the electron and hole concentrations on $x = 0$ and $x = b$ is a result

of the rapid spatial variation of the potential across the space-charge layers and band offsets at these interfaces.

The Boltzmann approximation for the carrier densities is accurate when the electron and hole densities are sufficiently high in the perovskite layer. This condition is met when the applied voltage is close to, or above, the cell's built-in voltage V_{bi}. Here, there is little potential drop to drive the carriers out of the perovskite layer (into transport layers), which, in turn, results in a substantial amount of free charge carriers remaining in the active layer. Thus at applied biases close to V_{bi} there are many more carriers present in the perovskite, than at lower biases (close to short-circuit). This enhances conductivity and, in turn, leads to the establishment of a quasi-equilibrium (i.e., Boltzmann) carrier distribution. An example of the extremely good agreement obtained between this approximation for the carrier densities and the full drift-diffusion model, as detailed in Eqs. (1)–(15) of [41], is shown in Fig. 3 which is computed for an IS voltage input of the form (1) with $V_{DC} = V_{OC}$ and $V_p = 10$ mV. Further verification of the Boltzmann approximation both at maximum power point and for a much reduced anion vacancy density of 1.6×10^{23} m^{-3} is made in Figs. S2 and S3, and once again shows good agreement with the approximation.

C. The current response during an IS experiment

The total current density flowing across the cell $J(t)$ is comprised of three components: the current generated by
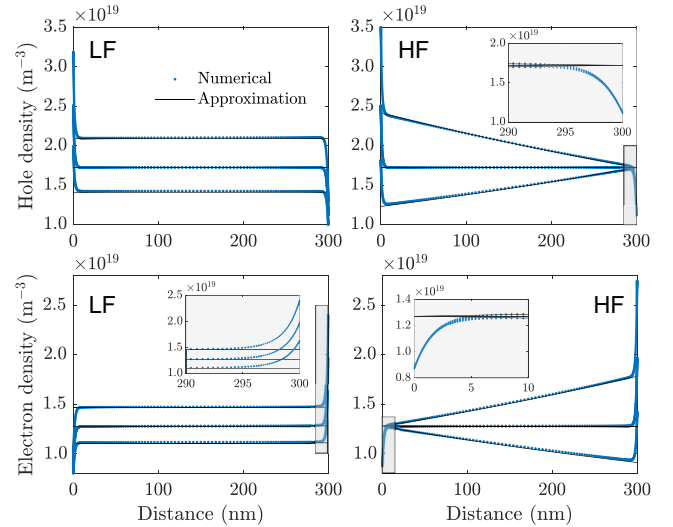

FIG. 3. Comparison between solutions obtained for the electron and hole densities from the full drift-diffusion model [Eqs. (1)–(15) of Ref. [41]] and the Boltzmann approximation. In both cases $V_{dc} = V_{OC}$. Left: carrier density at equally spaced intervals over a low-frequency period (1 mHz). Right: the equivalent but over an intermediate and high-frequency period (25 kHz). The parameters used are detailed in Table I, under 0.1-Sun equivalent illumination and with recombination at the ETL/perovskite interface (R_l) from Table II.

the incident radiation j_{gen}, the current loss due to charge-carrier recombination $-j_{\mathrm{rec}}$ and, at high frequencies, the displacement current j_d. In the usual fashion the charge conservation equation $\rho_t + j_x = 0$ can be expressed in terms of the displacement current j_d as follows:

$$\frac{\mathrm{d}}{\mathrm{d}x}(j + j_d) = 0, \quad \text{where} \quad j_d = \frac{\mathrm{d}D}{\mathrm{d}t}$$

and D is the electric displacement. This is trivially integrated to yield $j + j_d = J(t)$ for some temporal function $J(t)$. Since the current is measured in a part of the circuit, which is a good conductor, the electric displacement, and hence the displacement current also, are negligible. It follows that the measured current density is to a good approximation $J(t)$. Furthermore, $J(t)$ is most easily computed in the perovskite layer, where the electric field $E = E(t)$ is (approximately) spatially uniform. At high frequency the displacement current j_d in the perovskite becomes appreciable, and the measured current density $J(t)$ is thus found by summing j_d to the real current density j (in the perovskite), which itself is composed of a current generated by the incident radiation, j_{gen}, and the recombination current density, j_{rec}. This results in the following expression for the measured current density:

$$J(t) = j_{\mathrm{gen}} - j_{\mathrm{rec}} + j_d \quad \text{where} \quad j_d(t) = \varepsilon_p \frac{dE}{dt}, \quad (18)$$

in which ε_p is the perovskite permittivity. Here j_{gen} is computed from the Beer-Lambert law

$$j_{\mathrm{gen}} = qF_{\mathrm{ph}}\left(1 - e^{-\alpha b}\right), \quad (19)$$

in which F_{ph} is the intensity of the incident radiation, α is the absorption coefficient, and b is the thickness of the perovskite layer (more details of the cell parameters are given in Table I).

1. The recombination current

Given the approximate carrier distributions (14)–(16) the recombination current can be determined from the bulk recombination rate $R_{\mathrm{bulk}}(n,p)$, and the interfacial rates $R_l(n_{\mathrm{ETL}}^{(l)}, p^{(l)})$ (on the interface with the ETL) and $R_r(n^{(r)}, p_{\mathrm{HTL}}^{(r)})$ (on the interface with the HTL) as follows:

$$j_{\mathrm{rec}} = qR_l\left(n_{\mathrm{ETL}}^{(l)}(t), p^{(l)}(t)\right) + qR_r\left(n^{(r)}(t), p_{\mathrm{HTL}}^{(r)}(t)\right)$$
$$+ q\int_0^b R_{\mathrm{bulk}}\left(n(x,t), p(x,t)\right)dx. \quad (20)$$

In the case where there is a single dominant recombination mechanism, as in the examples given in Table SII within the Supplemental Material [64], it is demonstrated that the recombination current can be expressed in the form

$$j_{\mathrm{rec}}(t) = j_{R_i}\exp\left(-\frac{F_i(V_1, V_2, V_3, V_4)}{V_T} - \frac{b}{n_{\mathrm{el}}V_T}E(t)\right). \quad (21)$$

Here $F_i(V_1, V_2, V_3, V_4)$ (the potential barrier to recombination [38] for recombination type i, where $i = b, p, n, l$ or r), n_{el} (the *electronic* ideality factor) and j_{R_i} (the recombination current prefactor) all depend on the dominant recombination mechanism and, for the recombination mechanism stated in Table II, are presented in Table III. Notably, n_{el}, the *electronic* ideality factor, takes either the value 1 or 2 depending on the recombination mechanism and can thus be used as a diagnostic tool (just as the ideality factor is in conventional photovoltaics) in order to distinguish between different possible sources of recombination within the cell. Critically, all the ionic effects are contained in the function F_i so that n_{el} depends only upon purely electronic effects. While not explicitly shown in Eq. (21), the potential barrier to recombination F_i has a (slow) time dependence through the potential drops V_{1-4} as each are

TABLE II. List of all recombination types considered in this study, including their approximations and relevant parameter values. The intrinsic carrier density within the perovskite, given by $n_i = \sqrt{g_C g_V}\exp\left((E_V - E_C)/2V_T\right)$, is negligible relative to the bulk carrier densities under illumination. Assuming trap-state energies lie close to the center of the band gap, the parameters k_{1-4} are also negligible. The interfacial recombination rate equations are dependent on the carrier densities at the left and right interfaces defined by Eqs. (15) and (16), respectively.

Recombination	Full form	Approx.	Values
Bimolecular R_b	$R_{\mathrm{bulk}} = \beta\left(np - n_i^2\right)$	$R_{\mathrm{bulk}} \approx \beta np$	$\beta = 10^{-12}\ \mathrm{m^3\ s^{-1}}$
Hole-limited SRH R_p	$R_{\mathrm{bulk}} = \frac{np - n_i^2}{\tau_n p + \tau_p n + k_1}$	$R_{\mathrm{bulk}} \approx \frac{p}{\tau_p}$	$\tau_n = 3 \times 10^{-10}\mathrm{s}$ $\tau_p = 3 \times 10^{-8}\mathrm{s}$
Electron-limited SRH R_n	$R_{\mathrm{bulk}} = \frac{np - n_i^2}{\tau_n p + \tau_p n + k_2}$	$R_{\mathrm{bulk}} \approx \frac{n}{\tau_n}$	$\tau_n = 3 \times 10^{-8}\mathrm{s}$ $\tau_p = 3 \times 10^{-10}\mathrm{s}$
ETL/perovskite interfacial recombination R_l	$R_l = \frac{n_{\mathrm{ETL}}^{(l)} p^{(l)} - n_i^2/k_E}{p^{(l)}/v_{n_E} + n_{\mathrm{ETL}}^{(l)}/v_{P_E} + k_3}$	$R_l \approx v_{P_E} p^{(l)}$	$v_{n_E} = 10^5\ \mathrm{ms^{-1}}$ $v_{P_E} = 5\ \mathrm{ms^{-1}}$
Perovskite/HTL interfacial recombination R_r	$R_r = \frac{n^{(r)} p_{\mathrm{HTL}}^{(r)} - n_i^2/k_H}{p_{\mathrm{HTL}}^{(r)}/v_{n_H} + n^{(r)}/v_{P_H} + k_4}$	$R_r \approx v_{n_H} n^{(r)}$	$v_{n_H} = 5\ \mathrm{ms^{-1}}$ $v_{P_H} = 10^5\ \mathrm{ms^{-1}}$

TABLE III. Recombination types with labeling convention and corresponding values for the electronic ideality factor. $F_i(V_1, V_2, V_3, V_4)$ is the potential barrier to recombination for recombination of type R_i, where $i = b, p, n, l, r$. This notation enables the recombination current [Eq. (21)] and impedance parameters, Eqs. (22)–(25), to be written in a general form. The total potential drop across the cell at steady state is given by $V_1 + V_2 + V_3 + V_4 = V_{bi} - V_{dc}$.

R_i	Recombination	$F_i(V_1, V_2, V_3, V_4)$	j_{R_i}	n_{el}
R_b	$R_{bulk} = \beta np$	$V_1 + V_2 + V_3 + V_4$	$qb\beta k_E d_E k_H d_H$	1
R_p	$R_{bulk} = p/\tau_p$	$V_3 + V_4$	$\frac{qbk_H d_H}{\tau_p}$	2
R_n	$R_{bulk} = n/\tau_n$	$V_1 + V_2$	$\frac{qbk_E d_E}{\tau_n}$	2
R_l	$R_l = v_{p_E} p^{(l)}$	$V_2 + V_3 + V_4$	$qk_H d_H v_{p_E}$	1
R_r	$R_r = v_{n_H} n^{(r)}$	$V_1 + V_2 + V_3$	$qk_E d_E v_{n_H}$	1

a function of $Q(t)$. At steady state, Eq. (21) corresponds exactly to the ectypal diode equation given in Ref. [38]. Further discussion of the electronic ideality factor can be found in Secs. V and V A, along with details of how it may be obtained experimentally.

Throughout this work we focus primarily on cells in which there is a single dominant charge-carrier recombination mechanism and only briefly consider cells where more than one recombination mechanism is significant (the analysis for such cells is broadly similar but more complex).

2. Predicting impedance response from the linearized model

In scenarios where the magnitude of the voltage perturbation V_p is small (in comparison to the thermal voltage V_T) it is possible to linearize the model equations about the steady-state voltage V_{dc}. Obtaining solutions to this linearized model for a general IS voltage, Eq. (1), the current response of the cell can be expressed in the form of Eq. (3). The relative phase and amplitude of the sinusoidal current response is used to calculate the complex impedance as a function of perturbation frequency.

In turn, the impedance can be related to the equivalent *RC-RC* circuit depicted in Fig. 1(c). This enables the identification of the HF and LF resistances, R_{HF} and R_{LF}, and capacitances, C_{HF} and C_{LF}, of the cell. The complete derivation of this impedance model is provided in S2 within the Supplemental Material [64].

III. IMPEDANCE FORMULAE FROM THE ANALYTIC MODEL

On solution to the approximate model detailed in the previous section, it is found that the impedance response of a PSC can be related to an *RC-RC* equivalent circuit, as shown in Fig. 1(c), with the components defined in terms

of the following device properties:

$$R_{HF} = \frac{V_T n_{el}}{j_{rec}(V_{dc})}, \tag{22}$$

$$R_{LF} = \frac{V_T}{j_{rec}(V_{dc})} \left(n_{ap}(V_{dc}) - n_{el} \right), \tag{23}$$

$$C_{HF} = \frac{\varepsilon_p}{b}, \tag{24}$$

$$C_{LF} = \frac{n_{ap}(V_{dc}) j_{rec}(V_{dc})}{G_+ V_T n_{el} \left(n_{ap}(V_{dc}) - n_{el} \right)} \left(-\frac{dQ_{dc}}{dV_{dc}} \right). \tag{25}$$

Here $j_{rec}(V_{dc})$ is the steady-state recombination current density, ε_p is the perovskite layer permittivity, n_{ap} is the apparent ideality factor determined by the standard techniques used to obtain the ideality factor (such as the Suns-V_{OC} or dark-JV methods), n_{el} is the electronic ideality factor, and the parameter G_+ quantifies the ionic conductance per unit area of the perovskite layer and is given by

$$G_+ = \frac{q D_+ N_0}{V_T b}. \tag{26}$$

The final term in Eq. (25) is found by solving Eq. (13) to obtain an expression for Q_{dc} as a function of V_{dc} and then differentiating this function with respect to V_{dc}. Plots of Q_{dc} as a function of V_{dc} are made in Fig. S16(a) while those of its derivative dQ_{dc}/dV_{dc}, which appears in the expression for C_{LF}, can be found in Fig. S16(b). Notably $(-dQ_{dc}/dV_{dc})$ is the ionic capacitance of the cell (per unit area)

A. Interpretation of the results

Equations (22)–(25) illustrate how to interpret the impedance response of a PSC. In particular, they show that the impedance spectrum of the drift-diffusion model of a PSC is associated with two dominant features, a low- and a high-frequency one. Furthermore, since this response is closely related to that of the *RC-RC* circuit depicted in Fig. 1(c), it can be associated with two arcs in a Nyquist plot, as illustrated in Figs. 4 and 6, and equivalently two peaks in the frequency plots, as illustrated in Figs. 5 and 7. However, in contrast to a *RC-RC* circuit, the low-frequency capacitance and resistance are not guaranteed to be positive. In particular, in scenarios where $n_{el} > n_{ap}$ both R_{LF} and C_{LF} are negative (since dQ_{dc}/dV_{dc} is always negative while all the other terms in these formulae are positive). It is these negative capacitances and resistances that give rise to *so-called* inductive arcs in the Nyquist plot that appear below the axis, as, for example, in Fig. 6(b).

An alternative viewpoint is provided by starting from experimental IS data and using these data to obtain fits for $R_{HF}(V_{dc})$, $C_{HF}(V_{dc})$, $R_{LF}(V_{dc})$, and $C_{LF}(V_{dc})$. These experimentally derived expressions for the cell resistances and
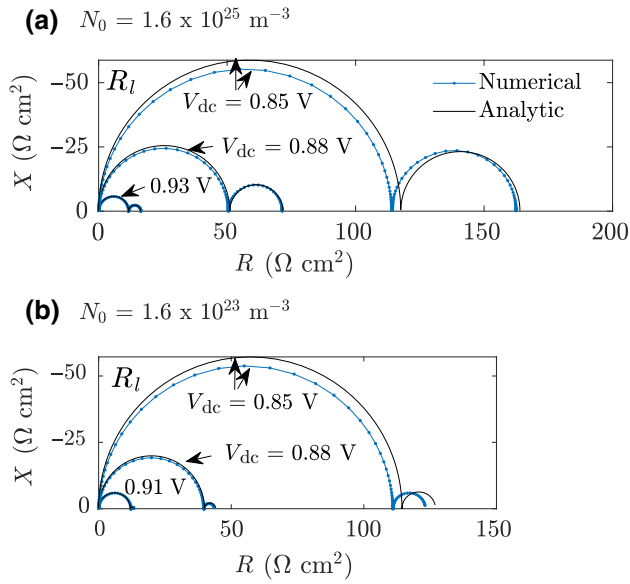
(a) $N_0 = 1.6 \times 10^{25}$ m^{-3}

(b) $N_0 = 1.6 \times 10^{23}$ m^{-3}

FIG. 4. Simulated impedance spectra for a PSC with recombination at the ETL/perovskite interface (R_l), under 0.1-Sun equivalent illumination and with different anion vacancy densities N_0. Spectra for three dc voltages are shown, including at open circuit, $V_{dc} = V_{OC}$ [i.e., 0.93 V in (a) and 0.91 V in (b)]. The impedance perturbation amplitude is 10 mV, recombination parameters are listed in Table II, while other cell parameters are listed in Table I. Frequency plots for (a),(b) are presented in Figs. 5 and S4 within the Supplemental Material [64], respectively.

capacitances can, in turn, be used to infer many of the cell's properties.

1. The apparent ideality factor

The unconventional physics of PSCs means that the value of n_{ap} cannot be related straightforwardly to the recombination mechanism, as is the case for a conventional
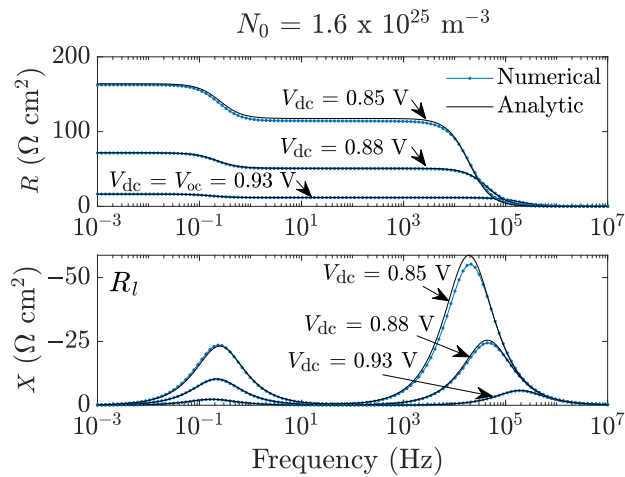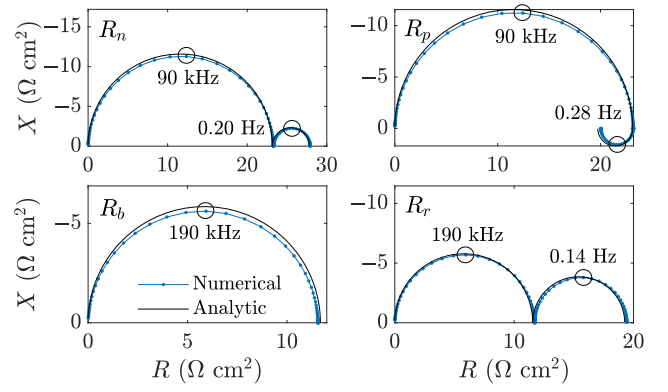

FIG. 6. Simulated impedance spectra at open circuit with different recombination mechanisms. R_n, electron-limited bulk SRH (V_{OC}=0.94 V); R_p, hole-limited bulk SRH (V_{OC}=0.92 V); R_b, bimolecular bulk recombination (V_{OC}=0.95 V); R_r, perovskite and HTL interfacial (V_{OC}=0.95 V). Cell and recombination parameters as listed in Tables I and II, respectively.

solar cell. Instead the apparent ideality factor determined for PSCs using standard techniques should be interpreted in terms of the model by the following approximate expression, which is exact for $V_{dc} = V_{bi}$, (for further details see Ref. [38], in which n_{ap} is referred to as the measured ectypal factor):

$$n_{ap}(V_{dc}) \approx \frac{V_{bi} - V_{dc}}{F_i(V_1(Q_{dc}), V_2(Q_{dc}), V_3(Q_{dc}), V_4(Q_{dc}))}. \quad (27)$$

Here we make use of the fact that $V_1(Q_{dc}) + V_2(Q_{dc}) + V_3(Q_{dc}) + V_4(Q_{dc}) = V_{bi} - V_{dc}$ and use the functional relation between the charge density and the applied voltage $Q_{dc} = Q_{dc}(V_{dc})$ that is obtained by inverting Eq. (13). Notably n_{ap} gives the ratio of the total potential drop across the cell $V_{bi} - V_{dc}$ to the potential barrier for recombination
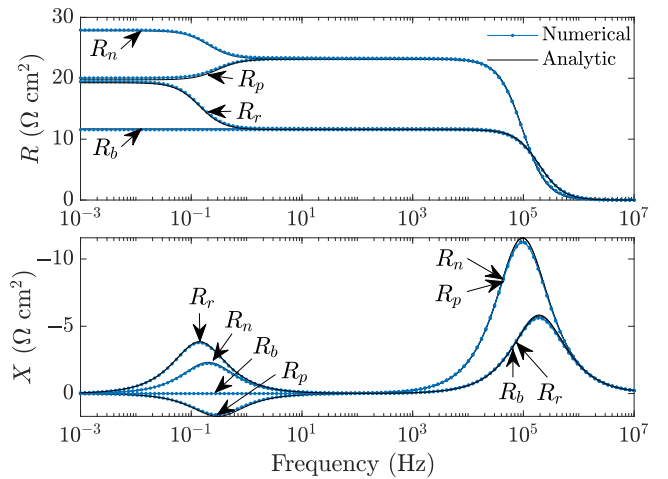

FIG. 5. Real (R) and imaginary (X) components of impedance versus frequency for the spectra presented in Fig. 4(a).

FIG. 7. Real (R) and imaginary (X) components of impedance versus frequency for the spectra presented in Fig. 6.

F_i. Furthermore, n_{ap} is inherently dependent on the applied voltage, the ion-vacancy density and transport layer properties, via Ω_E and Ω_H [as defined in Eq. (9)]. In scenarios where $n_{ap} = n_{el}$ the low-frequency arc of the Nyquist plot disappears, as can be seen from Eqs. (22)–(25). This situation, i.e., $n_{ap} = n_{el}$, occurs when there are no mobile ions (see Sec. V for further details) and a conventional (nonideal) diodic response is observed. However, it can also occur even in the presence of mobile ions, as, for example, when recombination occurs in the perovskite via a purely bimolecular mechanism (see also Sec. VI A 2), as illustrated in Fig. 6(c). Further properties of the apparent ideality factor are discussed in Secs. V and V A.

2. Estimating the recombination current

It is notable that j_{rec} depends both on the steady-state voltage V_{dc} and on how the potential difference across the cell is divided between the potential drops $V_1 - V_4$; it is thus sensitive to parameters, such as the transport layer doping densities, that alter the relative distribution of the overall potential drop across $V_1 - V_4$ [41]. In steady state, the recombination current can be related to the photogenerated current j_{gen} and the steady-state current output of the cell $J(V_{dc})$ by the expression

$$j_{rec}(V_{dc}) = j_{gen} - J(V_{dc}). \tag{28}$$

This allows the steady-state recombination current to be estimated from experimental measurements by making the assumption that $j_{gen} \approx J(V_{dc} = 0)$.

IV. NUMERICAL SOLUTIONS TO THE DRIFT-DIFFUSION MODEL

Solutions to the drift-diffusion model of the planar PSC [as detailed in Eqs. (1)–(15) of Ref. [41]] are obtained by using the open-source PSC simulation tool `IonMonger` [65]. This solves the fully coupled ionic-electronic drift-diffusion equations for a planar PSC with a single positively charged mobile ion-vacancy species and mobile charge carriers in the perovskite layer (as described in Ref. [41]). Impedance spectra are obtained by using `IonMonger` to solve the drift-diffusion model multiple times, over a range of frequencies ω, with the voltage input given by Eq. (1). Comparison of the resulting output current to Eq. (3) allows the complex impedance $Z(\omega, V_{dc})$ to be obtained as a function of the frequency ω. A detailed description of this method is provided in Riquelme *et al.* [9], where it is used to show that the drift-diffusion model (described above) reproduces the main features of impedance experiments conducted on PSCs. Impedance spectra are calculated, in this way, at a specified steady-state voltage V_{dc} (for example, $V_{dc} = V_{OC}$) using the full forms of the recombination mechanisms specified

in Table II. These spectra are compared to the corresponding analytic spectra reconstructed from the analytic expressions for the low- and high-frequency resistances and capacitances, Eqs. (22)–(25). The numerical and analytic impedance spectra presented in this work (unless otherwise stated) are simulated at open circuit under monochromatic (520 nm) illumination with intensity that produces a photocurrent equivalent to 0.1 Sun at AM1.5. Impedance spectra are composed of 128 and 256 frequencies for the numerical and analytic solutions, respectively, over a range of 10^{-3}–10^7 Hz. The voltage perturbation amplitude is 10 mV throughout.

A. Comparison between analytic impedance formulae and spectra computed from numerical solution to drift-diffusion model

Figures 4–7 compare the simulated PSC impedance spectra from the impedance formulae (22)–(25) (derived from the analytic model) to the spectra obtained via numerical solution to the full drift-diffusion model [see Eqs. (1)–(15) of Ref. [41]]. These results show examples of all five recombination mechanisms described in Table II and are all simulated under 0.1-Sun equivalent illumination, with an equilibrium vacancy density of $N_0 = 1.6 \times 10^{25}$ m^{-3}. In all cases the other parameter values are taken from Table I, with the exception of Fig. 4(b), which shows spectra at different dc voltages for a cell with a low vacancy density of $N_0 = 1.6 \times 10^{23}$ m^{-3}, comparable with the lower densities used by some other groups [29,66].

Notably the analytic impedance formulae are compatible with simulations of the full drift-diffusion model both in the case of the higher vacancy density $N_0 = 1.6 \times 10^{25}$ m^{-3}, and in that of the lower value $N_0 = 1.6 \times 10^{23}$ m^{-3}. The key requirement for the analytic approach to work is that the Debye length is much shorter than the width of the perovskite layer and, even in the case of the lower ion vacancy density this is around 50 nm, which is still significantly shorter than the width of the perovskite layer (300 nm).

Additional plots showing simulated impedance spectra at 1-Sun illumination and at $V_{dc} = V_{MPP}$ (i.e., the maximum power point) can be found in S3 within the Supplemental Material [64]. It is also demonstrated in Figs. S11 and S12 within the Supplemental Material [64] that the analytic model, and corresponding impedance formulae, works even in the case of a much thinner ETL with significantly lower doping than the parameter set listed in Table I. Finally, Fig. S14 within the Supplemental Material [64] shows the error of the analytic model with respect to numerical solutions at different dc voltages at 0.1-Sun equivalent illumination and in the dark.

The analytic model finds that the characteristic low and high frequencies, ω_{LF} and ω_{HF}, which give the locations of

the maxima in $X(\omega)$ (see Fig. 7), are given by

$$\omega_{\mathrm{LF}} = G_+ \frac{n_{\mathrm{el}}}{n_{\mathrm{ap}}(V_{\mathrm{dc}})} \left(-\frac{dQ_{\mathrm{dc}}}{dV_{\mathrm{dc}}} \right)^{-1}, \qquad (29)$$

$$\omega_{\mathrm{HF}} = \frac{b j_{\mathrm{rec}}(V_{\mathrm{dc}})}{\varepsilon_p V_T n_{\mathrm{el}}}, \qquad (30)$$

in which $dQ_{\mathrm{dc}}/dV_{\mathrm{dc}}$ is negative for all V_{dc}, as shown in Fig. S16 within the Supplemental Material [64]. These characteristic frequencies are related to the resistances and capacitances via $\omega_{\mathrm{LF}} = 1/(R_{\mathrm{LF}}C_{\mathrm{LF}})$ and $\omega_{\mathrm{HF}} = 1/(R_{\mathrm{HF}}C_{\mathrm{HF}})$. The characteristic frequency of the LF feature ω_{LF} is proportional to G_+, which quantifies the ionic conductance defined in Eq. (26). In particular, ω_{LF} increases with increased anion vacancy density, or mobility. Given that $n_{\mathrm{ap}}dQ_{\mathrm{dc}}/dV_{\mathrm{dc}}$ is not strongly temperature dependent, the activation energy extracted from the LF time constant is the result of the temperature dependence of $G_+(T)$. Many experimental works corroborate this fact [18,19,24,67].

Overall, it is clear that there is an extremely good agreement between the impedance spectra predicted by the analytic model and those predicted by the full drift-diffusion model. Furthermore, both approaches can be used to illustrate how different recombination mechanisms impact the shape and features of the impedance spectra. The ability of the impedance formulae, obtained from the analytic model, to closely reproduce the results of the numerical model validates the use of the surface polarization model [41,42,46] and the use of the Boltzmann approximation in the computation of carrier densities and recombination rates.

The key advantages of using the (approximate) analytic model and the corresponding impedance formulae, as opposed to the drift-diffusion model, to interpret impedance spectra are that (I) "trends" (such as the dependence of the spectra on illumination, open-circuit voltage, and steady-state voltage) observed in real spectra can be much more easily understood in terms of the analytic model than from numerical simulations of the drift-diffusion model and (II) key physical parameters of the device may be obtained much more easily from impedance data by comparing to the explicit formulae for n_{ap}, R_{HF}, C_{HF}, R_{LF}, and C_{LF}, generated by the analytic model, than by repeatedly solving the drift-diffusion model until a parameter set is found that matches the data.

V. THE ELECTRONIC IDEALITY FACTOR

Analysis of the PSC drift-diffusion model, conducted in Ref. [38], demonstrates that the ideality factor as conventionally defined, and determined by the Suns-V_{OC} or dark-JV methods, is dependent on the applied voltage (a consequence of ion motion) and should thus be interpreted

very differently to the traditional ideality factor. We therefore term this version of the ideality factor the apparent ideality factor, n_{ap}. However, in deriving the IS model presented here we also identify an alternative dimensionless parameter, which we term the *electronic ideality factor n_{el}*. This factor plays an analogous role in PSCs to that played by the traditional ideality factor in conventional photovoltaics and, in particular, can be used as a tool to deduce the dominant form of recombination taking place in the cell.

For the recombination mechanisms studied in this work (see Table II) the electronic ideality factor takes a value of either 1 or 2, depending on the dominant recombination mechanism. Specifically, it takes a value of 2 where recombination occurs via an electron-, or hole-, limited SRH mechanism within the perovskite absorber layer; and takes a value of 1 where bimolecular recombination in the perovskite is the dominant loss mechanism, or recombination occurs (via a SRH mechanism) on the interfaces with the transport layers. These results are stated in full in Table III. From an experimental perspective the electronic ideality factor can be determined from the high-frequency resistance and the recombination current [see Eqs. (22) and (28)] via the formula

$$n_{\mathrm{el}} = \frac{R_{\mathrm{HF}}(V_{\mathrm{dc}}) j_{\mathrm{rec}}(V_{\mathrm{dc}})}{V_T}, \qquad (31)$$

where j_{rec} may be estimated from Eq. (28). This result is key to analyzing the behavior of real cells from experimental data. The authors of this work have applied and tested Eq. (31) to derive the dominant recombination mechanism in triple-cation perovskite solar cells [68]. In particular, it is straightforward to obtain n_{el} since both $R_{\mathrm{HF}}(V_{\mathrm{dc}})$ and $j_{\mathrm{rec}}(V_{\mathrm{dc}})$ are readily measured. It is also the method used to determine n_{el} from impedance spectra generated by numerical simulation of the drift-diffusion model in Sec. V A.

In order to demonstrate how the model and the electronic ideality factor are related to conventional solar-cell theory, we consider a three-layer cell in which there are no mobile ions present in the perovskite capable of forming interfacial space-charge layers and screening the field from the absorber. In this scenario the interfacial potential drops are all zero, that is $V_1 = V_2 = V_3 = V_4 = 0$. The potential profile no longer has the form depicted in Fig. 2(a) but is instead similar to that typically portrayed for an ideal "*p-i-n*" junction, where the built-in voltage and applied potential is dropped uniformly across the central intrinsic (i.e., perovskite) layer. Hence, the uniform electric field in the perovskite [see Eq. (12)] is given by

$$E(t) = \frac{1}{b} (V_{\mathrm{bi}} - V(t)). \qquad (32)$$

Using the relation above, $V_{1-4} = 0$ and $F_i(V_{1-4}) = 0$, Eq. (21) for the recombination current simplifies to

$$j_{\text{rec}}(t) = j_{R_i}^* \exp\left(\frac{V(t)}{n_{\text{el}}V_T}\right), \tag{33}$$

where we define $j_{R_i}^* = j_{R_i} \exp(-V_{bi}/(n_{\text{el}}V_T))$. Ignoring the contribution from the displacement current, the total current is given by

$$J(t) = j_{\text{gen}} - j_{R_i}^* \exp\left(\frac{V(t)}{n_{\text{el}}V_T}\right). \tag{34}$$

This can be compared to the classical nonideal diode equation [30]

$$J(t) = j_{\text{gen}} - j_{g,\text{therm}} \exp\left(\frac{V(t)}{n_{\text{id}}V_T}\right), \tag{35}$$

where here $j_{\text{gen}} = j_{g,\text{sol}} + j_{g,\text{therm}}$ incorporates both solar $j_{g,\text{sol}}$ and thermal $j_{g,\text{therm}}$ generation terms. It is clear from this comparison that, in the absence of ions in the perovskite layer, the electronic ideality factor is exactly analogous to the ideality factor that appears in standard semiconductor diode theory. Finally, by removing the ions in this way it is evident, from Eqs. (22)–(25), that the LF impedance response disappears, leaving only the HF semicircle.

We derive an alternative form of ideality factor, namely the electronic ideality factor n_{el}, that is appropriate for analyzing the behavior of a PSC. In contrast to the apparent ideality factor n_{ap}, which is commonly used to analyze PSC behavior in the literature, the electronic ideality factor is not inherently voltage dependent and is not influenced by the distribution of potential drops V_{1-4} across the cell. More specifically, it is a purely electronic parameter, which is not influenced by the physical behavior of the ions in the perovskite material. In order to justify this assertion we note that n_{el} is obtained using only the high-frequency impedance measurements, via Eq. (31). At high frequencies, the cell is perturbed about its steady-state ionic configuration and the ions are effectively immobile, because they move too slowly to respond to the voltage oscillations. As a result, the perturbed potential is only dropped across the interior of the perovskite layer, to produce an oscillating internal electric field, which modulates only the electron and hole densities (this is illustrated in Fig. 10). Even at these high frequencies, the electron and hole concentrations remain in quasiequilibrium. As such, only HF impedance is capable of probing the electronic properties of a PSC about a particular steady state. Although the drift-diffusion model of a PSC leads us to conclude, at least where there is only a single source of recombination, that n_{el} is independent of applied voltage it is, from a practical perspective, probably best practice to determine n_{el}

from experiments conducted at the maximum power point as this provides the best picture of the cell working under typical operating conditions.

A. Comparison between electronic and apparent ideality factors

On referring to Eqs. (22)–(25) it is clear that the apparent ideality factor can be written in the form

$$n_{\text{ap}}(V_{\text{dc}}) = \frac{j_{\text{rec}}(V_{\text{dc}})}{V_T}\left(R_{\text{HF}}(V_{\text{dc}}) + R_{\text{LF}}(V_{\text{dc}})\right), \tag{36}$$

which gives a method for obtaining the apparent ideality factor n_{ap} from IS data without having to determine the gradient of a linear fitted function (as is required by the Suns-V_{OC}, dark-JV, and $R_{\text{HF}} - V_{\text{OC}}$ techniques). Notably, once n_{ap} has been determined, it can be used to estimate the potential barrier for recombination F_i at steady state by inverting the formula (27) to obtain

$$F_i|_{V_{\text{dc}}} \approx \frac{V_{\text{bi}} - V_{\text{dc}}}{n_{\text{ap}}(V_{\text{dc}})}, \tag{37}$$

which is accurate when V_{dc} is near V_{bi} (note that in the limit $V_{\text{dc}} \to V_{\text{bi}}$, $F_i \to 0$ and n_{ap} is well defined). For further details see Ref. [38].

In Fig. 8, the electronic ideality factor n_{el} and the apparent ideality factor n_{ap} are computed using Eqs. (31) and (36), and plotted against the open-circuit voltage V_{OC},
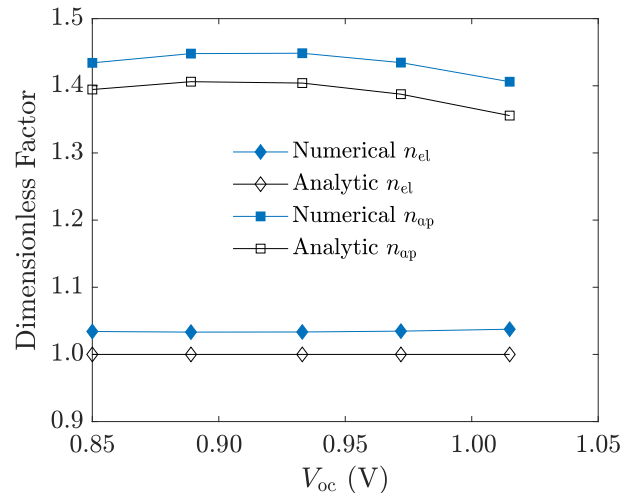
FIG. 8. Electronic ideality factor, n_{el}, and apparent ideality factor, n_{ap}, calculated at different open-circuit voltages (corresponding to different illumination intensities) from impedance spectra obtained analytically and numerically. Calculated from the same spectra as used for Fig. S13(f) within the Supplemental Material [64]. Parameters used to calculate the numerical and analytic spectra are those from Table I for a cell with hole-limited interfacial recombination (R_l).

as the illumination intensity is varied. In the analytic computation of the ideality factors the low- and high-frequency resistances are determined using the formulae (22)–(23) while the recombination current j_{rec} is computed from Eq. (21). In contrast, in the case of the numerical computation, the resistances are calculated by fitting numerically generated impedance spectra to an *RC-RC* equivalent circuit while j_{rec} is computed from Eq. (28).

The results show the voltage independence of n_{el}, for a single dominant source of recombination and, additionally, demonstrates that a noninteger value of n_{ap} is obtained, even in cells with a single (monomolecular) recombination mechanism. This supports the interpretation of n_{ap} as an apparent ideality factor rather than a true ideality factor.

In order to highlight the difference between the apparent and electronic ideality factors we compute these quantities under 0.1-Sun illumination and at V_{OC} for the five different forms of recombination detailed in Table II and for the cell described in Sec. VI B with multiple recombination mechanisms. The results of these computations are displayed in Fig. 9. We remark that while n_{ap} for this cell lies within the range that typically would be expected for an ideality factor (i.e., mainly between 1 and 2) it is highly sensitive to device parameters (such as ion density or transport layer doping, see, for example, Ref. [9]) and for certain cell parameter sets n_{ap} would lie well outside this range. It is clear from Fig. 9 that the factors calculated from the drift-diffusion model closely match those predicted by the analytic model (at V_{OC}). Even where only a single source of recombination is present the apparent ideality factor n_{ap} is noninteger (except for purely bimolecular recombination). This highlights the challenge of attributing a particular form of recombination to a value of n_{ap}. In contrast, however, where a single recombination mechanism
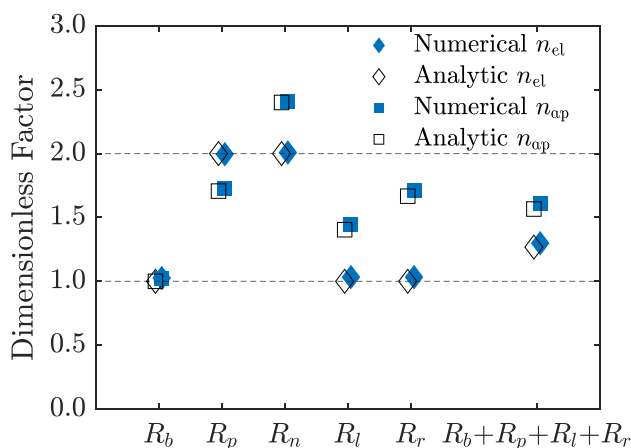

FIG. 9. Electronic ideality factor and the apparent ideality factor calculated from impedance spectra at open circuit for the five recombination types considered in this work and cell parameters from Table I. The rightmost entry is for multiple recombination mechanisms, as displayed in Fig. 12.

dominates, the electronic ideality factor n_{el} is an integer and its value can be used to distinguish between bulk SRH recombination $n_{el} = 2$ and interfacial recombination $n_{el} = 1$. For multiple recombination mechanisms, the electronic ideality factor quantifies the proportion of bulk SRH to interfacial (and bimolecular) recombination via Eq. (39). If the size and proportion of some of the potentials V_{1-4} are known it is then theoretically possible, by pairing this information about n_{el} and n_{ap} [using Eq. (27)], to diagnose the exact form and location of the recombination which is limiting cell performance. For instance, we showed recently (Castro-Chong *et al.* [68]) that by monitoring the electronic ideality factor as computed with Eq. (31) and using experimental impedance data, that a change of recombination mechanism can be detected when the illumination intensity is increased in triple cation solar cells. This shows the usefulness of the proposed method to separate ionic effects from pure electronic recombination properties.

VI. DISCUSSION

In this section the implications of the analytic theory to real impedance experiments are discussed and, in Sec. VI B, the extension to the theory to scenarios in which there are multiple sources of recombination is briefly touched upon.

A. Qualitative behavior of the impedance response
1. High-frequency feature.

The analytic and numerical results show a high-frequency feature in the form of a semicircle above the axis on a Nyquist plot. This is consistent across all recombination types (light intensities and dc voltages) and matches that reported in experiment [18,19,33,69]. Notably the effects of the contacts and the measurement apparatus used to obtain IS measurements are not included in these models. Typically these lead to an additional series resistance whose effect is to shift the spectra along the real (R) axis in the Nyquist plane. Unlike many other measurement techniques, high-frequency impedance removes the transient effects of ion motion and leads to a response that is determined solely by the electronic properties of the PSC. The typical evolution of the potential in a device, over a period of a high-frequency impedance measurement (greater than approximately 100 Hz), is illustrated in Fig. 10. Further details of the HF response can be found in Riquelme *et al.* [9].

The impedance formulae (obtained from the analytic model) identify the high-frequency resistance [via Eqs. (24)–(25)] as inversely proportional to the recombination current. This is in line with the usual interpretation of a recombination resistance [37,70]. In addition, it identifies the high-frequency capacitance [see Eqs. (24)–(25)]
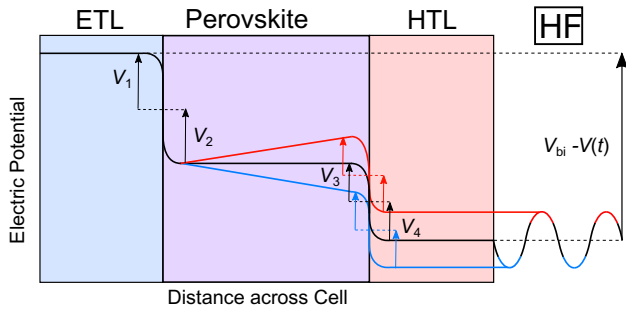
FIG. 10. Illustration of the potential across a PSC during high-frequency (above approximately 100 Hz) impedance measurements. The ion distribution is unable to adjust over the short timescale of a period and so the potential drops across the space-charge layers V_{1-4} remain in their steady-state configuration. Therefore, at high frequencies the applied voltage results in an approximately uniform oscillating electric field $E(t)$ across the perovskite.
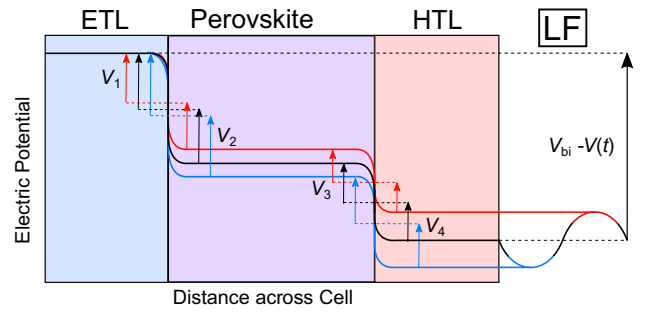

FIG. 11. Illustration of the effect of an oscillating potential difference on the distribution of the electric potential across a PSC during impedance measurements at ultralow frequencies (below approximately 10 mHz). The slow modulation of applied voltage allows ionic charge to fill and deplete the perovskite space-charge layers in phase with the applied potential. The charging and discharging of space-charge layers effectively screens the bulk electric field.

as a purely geometric capacitance [23,71], which is consistent with other reports found in the literature [18,19,28,37,70–73]. This is a consequence of the contribution to the total current from the out-of-phase displacement current caused by polarization of the perovskite layer, and given by Eq. (18).

Calculating the geometric capacitance from the perovskite permittivity and perovskite width returns capacitances up to 10–100 times less than those extracted experimentally. In order to reconcile this discrepancy between the geometric capacitance predicted by the thickness and permittivity of the perovskite absorber layer and experimentally measured value of C_{HF} a roughness factor has been proposed, which accounts for the nonplanar (rough) nature of the perovskite transport layer interfaces [9,37]. The low values of C_{HF} obtained from our simulations (in both numerical and analytic impedance spectra calculated without a roughness factor) are reflected in the frequency plots, which show that the HF peak is shifted to slightly higher frequencies than is measured in experiment [18,19].

2. Low-frequency feature

At low frequency, the possible impedance response of a PSC can be more varied. The analytic model shows that, depending upon the cell parameters, three different LF responses may be observed in the Nyquist plane. Either, (1) no visible LF feature or (2) a "capacitive" semicircle above the axis, or (3) an "inductive" semicircle below the axis. These different LF features are displayed in Figs. 6 and S7 within the Supplemental Material [64]. The time constant associated with the low frequency process is around 1-10 s, which is in line with experimental reports [18–20].

In the ultralow-frequency limit (below approximately 10^{-2} Hz), the modulation of the applied potential is so slow that the ionic distribution remains in approximate

quasiequilibrium throughout the perturbation and, as a result, the electric field within the perovskite layer is almost entirely screened [i.e., $E(t) \approx 0$], as illustrated in Fig. 11. More generally, the LF response results in only partial screening of the electric field from the perovskite because the flow of charge, into and out of the space-charge layers, lags behind the oscillating potential. During a LF measurement the evolving potential drops across the space-charge layers $V_{1-4}(t)$ modulate the recombination current (21) and thus lead to an impedance response that is dependent on the properties of the ion motion, an interpretation that is in line with the discussions of IS in PSCs found in Refs. [18,27,28].

The forms of the relations for R_{LF} and C_{LF}, given in Eqs. (22)–(25), provide insight into why certain features are observed in the IS response of a PSC. For example, when the recombination in a cell is dominated by bimolecular recombination, the low-frequency resistance shrinks to zero (since in this scenario $n_{ap} = n_{el} = 1$), so that only a high-frequency semicircle is observed in the Nyquist plot as, for example, shown in Fig. 6(c). While it is not realistic to entirely eliminate all other sources of recombination, this result is nevertheless interesting, since it demonstrates that the absence of a LF arc does not necessarily signify the absence of ion motion. Indeed the LF feature may also disappear where other types of recombination are present if $n_{ap} = n_{el}$, see Table IV for further details.

The condition for the low-frequency feature to appear "inductive" (i.e., to lie below the axis on a Nyquist plot) is that both $R_{LF} < 0$ and $C_{LF} < 0$ and, as can be seen from Eqs. (22)–(25), this occurs when

$$n_{ap} < n_{el}. \qquad (38)$$

More details about when such an "inductive" arc can be expected to appear, for the particular types of

TABLE IV. Table showing the relationship between recombination mechanism and observed low-frequency features. These conditions are derived using the inequality (38) and the expression for n_{ap} in Eq. (27) and assuming V_{dc} is sufficiently close to V_{bi}, see Ref. [38]. Table S3 within the Supplemental Material [64] gives equivalent conditions where V_{dc} lies further away from V_{bi}.

Rec.	Condn.s no LF feature	Possible R_{LF} & C_{LF} negative?
R_b	always (since $n_{ap} = n_{el}$)	No ($R_{LF} = 0$, $C_{LF} = \infty$)
R_p	if $V_1 + V_2 = V_3 + V_4$	Yes if $V_1 + V_2 < V_3 + V_4$
R_n	if $V_1 + V_2 = V_3 + V_4$	Yes if $V_3 + V_4 < V_1 + V_2$
R_l	if $V_1 << V_2 + V_3 + V_4$	No ($R_{LF} \geq 0$, $C_{LF} > 0$)
R_r	if $V_4 << V_1 + V_2 + V_3$	No ($R_{LF} \geq 0$, $C_{LF} > 0$)

recombination considered here, are provided in Table IV. A notable result is that an "inductive" arc in the LF feature never occurs where the recombination occurs predominantly on one of the interfaces with the transport layers. Reframing this point, if a negative low-frequency feature is observed in a Nyquist plot, we can infer from the model that the dominant recombination mechanism is bulk SRH within the perovskite layer.

B. General recombination mechanisms

Up until now we consider only scenarios where there is a single recombination mechanism. Whilst this is, in general, unrealistic there is usually a dominant form of recombination for any particular applied voltage V_{dc}, and therefore for any given impedance measurement. The results from one of these simple cases, with a single recombination mechanism, is therefore likely to give a good qualitative understanding of any particular impedance measurement conducted on a PSC. Nevertheless, it is possible to generalize the analytic impedance model to describe cells with any combination of recombination mechanisms. We are therefore not restricted solely to considering the forms found in Table II. However, the more general sets of recombination mechanisms lead to unwieldy expressions for the HF and LF resistances and capacitances that are less easily interpreted.

In order to illustrate the sort of behavior that might be expected in a real cell we provide a representative example of a PSC with the combination of the recombination pathways given in Table II. In particular, we assume the additive combination $R_b + R_p$ of bimolecular and hole-limited recombination in the perovskite, as given in Table II, and the surface recombination pathways R_l (on the ETL/perovskite interface) and R_r (on the perovskite/HTL interface), again as given in Table II. The analytic results for this cell [determined from Eqs. (S87)–(S88)] are compared to the numerical solutions to the drift-diffusion model, in which the full recombination rates are used. Figure 12 shows a comparison
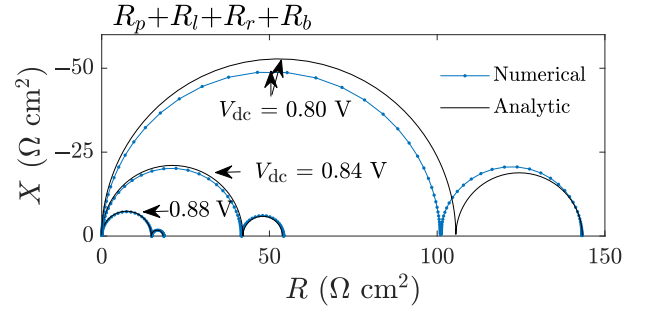

FIG. 12. Simulated impedance spectra for a PSC with four types of recombination under 0.1-Sun equivalent illumination. Spectra at three dc voltages are shown, including $V_{OC} = 0.88$ V. Specifically, the recombination taking place is bimolecular (R_b) and hole-limited SRH (R_p) in the bulk and at both the ETL/perovskite (R_l) and perovskite/HTL (R_r) interfaces. Recombination parameters for each type are specified in Table II and the additional parameters are given in Table I. Figure S9 within the Supplemental Material [64] presents the corresponding frequency plot for this Nyquist diagram.

between the two approaches for this cell (i.e., analytic model versus drift-diffusion model) and demonstrates good agreement between the two approaches across the full frequency range. The corresponding frequency plots are presented in Fig. S9 within the Supplemental Material [64]. As expected, this combination of different recombination mechanisms leads to a decrease in open-circuit voltage (V_{OC}=0.88 V for $R_p + R_l + R_r + R_b$ as compared to V_{OC}=0.93 V with just R_l).

For a cell with multiple recombination pathways the interpretation of the high- and low-frequency features remains the same. However, interpretation of the electronic ideality factor and the apparent ideality factor, calculated using Eqs. (31) and (36), respectively, is a little more complicated. We show in Eq. (S97) within the Supplemental Material [64], that for a cell with multiple recombination pathways, the electronic ideality factor is given by

$$ n_{el} = \frac{2}{2 - r_{SRH}}, \qquad (39) $$

where r_{SRH} is the ratio of the SRH recombination current to the total recombination current. Therefore, the electronic ideality factor, calculated from an impedance spectrum using Eq. (31), lies close to 1 when SRH recombination is negligible relative to interfacial (or bimolecular) recombination. Correspondingly, a value for the electronic ideality factor that is close to 2 indicates that the dominant form of recombination is SRH in the perovskite. In the following section we compare the values of the electronic ideality factor to those of the apparent ideality factor for various types of recombination.

Further information on interpreting impedance spectra is to be found in S4 within the Supplemental Material [64]

with examples on how to apply the formulae (22)–(25) in specific scenarios.

VII. CONCLUSIONS

In this work we derive an approximate analytic model (i.e., one based on a set of transcendental equations as opposed to a set of differential equations), and corresponding impedance formulae, for the impedance response of a PSC from a commonly used drift-diffusion model of such devices [see Eqs. (1)–(15) of Ref. [41]], which includes the effects of halide ion vacancies and charge-carrier motion. We show excellent agreement between the solutions of the analytic model and the drift-diffusion model for impedance simulations conducted on a physically realistic set of parameters at V_{OC} and very good agreement at the maximum power point. It is significant that no fitting is required in order to obtain this agreement between the analytic model and the drift-diffusion model; they require only that the same set of physical parameters are used in both. Simulations using both the analytic and the drift-diffusion model show good qualitative agreement with experimental IS studies and are able to predict some of the surprising features that are seen in the literature, such as "negative" low-frequency arcs (which appear below the axis in Nyquist plots) and "giant low-frequency capacitance."

An equivalent circuit model for the IS response of a PSC is derived systematically from a drift-diffusion theory that incorporates the physics of mobile ion vacancies. The impedance formulae obtained from the analytic model justify the use of an *RC-RC* equivalent circuit to fit to experimental PSC impedance spectra and defines the resistances and capacitances extracted from spectra in terms of physical cell properties. The model Eqs. (22)–(25) show exactly how to interpret the features, including the negative LF "resistances" and "capacitances." It is found that near open circuit the shape of the spectra is related to the type of recombination losses, through the values of the apparent n_{ap} and electronic ideality factors n_{el}.

From a practical perspective, probably the key result of this work is the identification of an alternative ideality factor that is appropriate for analyzing the behavior of PSCs. This can be determined from the high-frequency resistance and the recombination current via the relation [see Eq. (31)]

$$n_{el} = \frac{R_{HF}(V_{dc})j_{rec}(V_{dc})}{V_T}, \tag{40}$$

and has the property that, provided the dominant source of recombination does not alter as the steady-state applied voltage V_{dc} is changed, it is independent of V_{dc}. This is a consequence of its dependency on electronic, rather than ionic, parameters. This is in stark contrast to the standard form of the ideality factor, which is determined from

experiments such as Suns-V_{OC}, and which we term here the apparent ideality factor n_{ap}. This varies both with changes in V_{dc}, and (rather strongly) with changes in ionic parameters such as the ion concentration. Crucially, where there is a single dominant source of recombination loss within the cell, n_{el} takes an integer value. In particular, if this dominant loss mechanism occurs via SRH recombination within the perovskite layer then $n_{el} = 2$, whereas if the dominant loss mechanism occurs via interfacial recombination on one of the interfaces between the perovskite and transport layers then $n_{el} = 1$.

It is worthwhile to note that there are some physical limitations to the analytic model that we derive. Chief amongst these is that it is reliant on the charge carriers being close to quasiequilibrium, so that, in this particular instance, they are close to being Boltzmann distributed. This approximation works well if there are sufficient carriers in the device to easily transport the current being extracted from it. In practice, this means that it works very well in a region close to V_{OC}, which extends to the maximum power point, where there is little resistance to flow of out of the perovskite absorber layer, but it breaks down as the bias is reduced towards short circuit.

Finally, we remark on the generality of the approach that is adopted to arrive at the analytic model. Although we apply only this model to the standard perovskite drift-diffusion model of a PSC, with mobile charge carriers and a single mobile ion species, it is easily extended to other drift-diffusion-type models that might be applied to such cells. For example, it is currently believed that a second very slow mobile ion species may play a significant role in PSC physics and, in Ref. [51], an appropriate PSC drift-diffusion model is formulated that encapsulates this mechanism. There is also speculation that high doping in the transport layers may significantly alter the statistics of the charge carriers in these regions, especially where they are made from organic semiconducting materials, so that rather than being Boltzmann distributed they obey a Gauss-Fermi distribution [74,75]. In such scenarios the resulting drift-diffusion model of the PSC is modified but it will still be possible to apply the same techniques used here to arrive at an approximate analytic model of the IS response. Indeed, it should be noted that our approach can be applied more widely to other devices based on mixed ionic-electronic semiconductors.

---

[1] M. Green, E. Dunlop, J. Hohl-Ebinger, M. Yoshita, N. Kopidakis, and X. Hao, Solar cell efficiency tables (version 57), Prog. Photovoltaics: Res. Appl. **29**, 3 (2021).

[2] M. Jeong, I. W. Choi, E. M. Go, Y. Cho, M. Kim, B. Lee, S. Jeong, Y. Jo, H. W. Choi, J. Lee, Jin-Hyuk Bae, Sang Kyu Kwak, Dong Suk Kim, and Changduk Yang, Stable perovskite solar cells with efficiency exceeding 24.8% and 0.3-V voltage loss, Science **369**, 1615 (2020).

[3] N. R. E. Laboratory, NREL, Best Research-Cell Efficiency Chart, https://www.nrel.gov/pv/cell-efficiency.html (2020).

[4] T. A. Berhe, W.-N. Su, C.-H. Chen, C.-J. Pan, J.-H. Cheng, H.-M. Chen, M.-C. Tsai, L.-Y. Chen, A. A. Dubale, and B.-J. Hwang, Organometal halide perovskite solar cells: Degradation and stability, Energy. Environ. Sci. **9**, 323 (2016).

[5] E. Unger, G. Paramasivam, and A. Abate, Perovskite solar cell performance assessment, J. Phys.: Energy **2**, 044002 (2020).

[6] M.-C. Kim, S.-Y. Ham, D. Cheng, T. A. Wynn, H. S. Jung, and Y. S. Meng, Advanced characterization techniques for overcoming challenges of perovskite solar cell materials, Adv. Energy Mater. **11**, 2001753 (2020).

[7] S. Zhang, K. Xu, and T. Jow, EIS study on the formation of solid electrolyte interface in Li-ion battery, Electrochim. Acta **51**, 1636 (2006).

[8] E. Guillén, L. M. Peter, and J. Anta, Electron transport and recombination in ZnO-based dye-sensitized solar cells, J. Phys. Chem. C **115**, 22622 (2011).

[9] A. Riquelme, L. J. Bennett, N. E. Courtier, M. J. Wolf, L. Contreras-Bernal, A. B. Walker, G. Richardson, and J. A. Anta, Identification of recombination losses and charge collection efficiency in a perovskite solar cell by comparing impedance response to a drift-diffusion model, Nanoscale **12**, 17385 (2020).

[10] D. Klotz, G. Tumen-Ulzii, C. Qin, T. Matsushima, and C. Adachi, Detecting and identifying reversible changes in perovskite solar cells by electrochemical impedance spectroscopy, RSC Adv. **9**, 33436 (2019).

[11] C. Aranda, J. Bisquert, and A. Guerrero, Impedance spectroscopy of perovskite/contact interface: Beneficial chemical reactivity effect, J. Chem. Phys. **151**, 124201 (2019).

[12] A. Rizzo, F. Lamberti, M. Buonomo, N. Wrachien, L. Torto, N. Lago, S. Sansoni, R. Pilot, M. Prato, N. Michieli, Moreno Meneghetti, Gaudenzio Meneghesso, and Andrea Cester, Understanding lead iodide perovskite hysteresis and degradation causes by extensive electrical characterization, Solar Energy Mater. Solar Cells **189**, 43 (2019).

[13] A. Guerrero, J. You, C. Aranda, Y. S. Kang, G. Garcia-Belmonte, H. Zhou, J. Bisquert, and Y. Yang, Interfacial degradation of planar lead halide perovskite solar cells, ACS Nano **10**, 218 (2016).

[14] K. Domanski, J.-P. Correa-Baena, N. Mine, M. K. Nazeeruddin, A. Abate, M. Saliba, W. Tress, A. Hagfeldt, and M. Grätzel, Not all that glitters is gold: Metal-migration-induced degradation in perovskite solar cells, ACS Nano **10**, 6306 (2016).

[15] S. A. Weber, I. M. Hermes, S.-H. Turren-Cruz, C. Gort, V. W. Bergmann, L. Gilson, A. Hagfeldt, M. Graetzel, W. Tress, and R. Berger, How the formation of interfacial charge causes hysteresis in perovskite solar cells, Energy Environ. Sci. **11**, 2404 (2018).

[16] C. M. Wolff, P. Caprioglio, M. Stolterfoht, and D. Neher, Nonradiative recombination in perovskite solar cells: The role of interfaces, Adv. Mater. **31**, 1902762 (2019).

[17] B. Hailegnaw, N. S. Sariciftci, and M. C. Scharber, Impedance spectroscopy of perovskite solar cells: Studying the dynamics of charge carriers before and after continuous operation, Phys. Status Solidi A **217**, 2000291 (2020).

[18] A. Pockett, G. E. Eperon, N. Sakai, H. J. Snaith, L. M. Peter, and P. J. Cameron, Microseconds, milliseconds and seconds: Deconvoluting the dynamic behaviour of planar perovskite solar cells, Phys. Chem. Chem. Phys. **19**, 5959 (2017).

[19] L. Contreras-Bernal, S. Ramos-Terrón, A. Riquelme, P. P. Boix, J. Idígoras, I. Mora-Seró, and J. A. Anta, Impedance analysis of perovskite solar cells: A case study, J. Mater. Chem. A **7**, 12191 (2019).

[20] H. Wang, A. Guerrero, A. Bou, A. M. Al-Mayouf, and J. Bisquert, Kinetic and material properties of interfaces governing slow response and long timescale phenomena in perovskite solar cells, Energy Environ. Sci. **12**, 2054 (2019).

[21] E. Ghahremanirad, A. Bou, S. Olyaee, and J. Bisquert, Inductive loop in the impedance response of perovskite solar cells explained by surface polarization model, J. Phys. Chem. Lett. **8**, 1402 (2017).

[22] S. Ravishankar, C. Aranda, S. Sanchez, J. Bisquert, M. Saliba, and G. Garcia-Belmonte, Perovskite solar cell modeling using light-and voltage-modulated techniques, J. Phys. Chem. C **123**, 6444 (2019).

[23] A. Guerrero, G. Garcia-Belmonte, I. Mora-Sero, J. Bisquert, Y. S. Kang, T. J. Jacobsson, J.-P. Correa-Baena, and A. Hagfeldt, Properties of contact and bulk impedances in hybrid lead halide perovskite solar cells including inductive loop elements, J. Phys. Chem. C **120**, 8023 (2016).

[24] R. García-Rodríguez, D. Ferdani, S. Pering, P. J. Baker, and P. J. Cameron, Influence of bromide content on iodide migration in inverted MAPb(I$_{1-x}$Br$_x$)$_3$ perovskite solar cells, J. Mater. Chem. A **7**, 22604 (2019).

[25] A. O. Alvarez, R. Arcas, C. A. Aranda, L. Bethencourt, E. Mas-Marzá, M. Saliba, and F. Fabregat-Santiago, Negative capacitance and inverted hysteresis: Matching features in perovskite solar cells, J. Phys. Chem. Lett. **11**, 8417 (2020).

[26] F. Ebadi, N. Taghavinia, R. Mohammadpour, A. Hagfeldt, and W. Tress, Origin of apparent light-enhanced and negative capacitance in perovskite solar cells, Nat. Commun. **10**, 1 (2019).

[27] D. Moia, I. Gelmetti, P. Calado, W. Fisher, M. Stringer, O. Game, Y. Hu, P. Docampo, D. Lidzey, E. Palomares, Jenny

Nelson, and Piers R. F. Barnes, Ionic-to-electronic current amplification in hybrid perovskite solar cells: Ionically gated transistor-interface circuit model explains hysteresis and impedance of mixed conducting devices, Energy Environ. Sci. **12,** 1296 (2019).

[28] D. A. Jacobs, H. Shen, F. Pfeffer, J. Peng, T. P. White, F. J. Beck, and K. R. Catchpole, The two faces of capacitance: New interpretations for electrical impedance measurements of perovskite solar cells and their relation to hysteresis, J. Appl. Phys. **124,** 225702 (2018).

[29] M. T. Neukom, A. Schiller, S. Züfle, E. Knapp, J. Ávila, D. Pérez-del Rey, C. Dreessen, K. P. Zanoni, M. Sessolo, H. J. Bolink, and Beat Ruhstaller, Consistent device simulation model describing perovskite solar cells in steady-state, transient, and frequency domain, ACS Appl. Mater. Interfaces **11,** 23320 (2019).

[30] J. Nelson, *The Physics of Solar Cells* (World Scientific Publishing Company, London, 2003).

[31] P. Caprioglio, C. M. Wolff, O. J. Sandberg, A. Armin, B. Rech, S. Albrecht, D. Neher, and M. Stolterfoht, On the origin of the ideality factor in perovskite solar cells, Advan. Energy Mater. **10,** 2000502 (2020).

[32] P. Calado, D. Burkitt, J. Yao, J. Troughton, T. M. Watson, M. J. Carnie, A. M. Telford, B. C. O'Regan, J. Nelson, and P. R. Barnes, Identifying Dominant Recombination Mechanisms in Perovskite Solar Cells by Measuring the Transient Ideality Factor, Phys. Rev. Appl. **11,** 044005 (2019).

[33] O. Almora, K. T. Cho, S. Aghazada, I. Zimmermann, G. J. Matt, C. J. Brabec, M. K. Nazeeruddin, and G. Garcia-Belmonte, Discerning recombination mechanisms and ideality factors through impedance analysis of high-efficiency perovskite solar cells, Nano Energy **48,** 63 (2018).

[34] W. Tress, M. Yavari, K. Domanski, P. Yadav, B. Niesen, J. P. C. Baena, A. Hagfeldt, and M. Graetzel, Interpretation and evolution of open-circuit voltage, recombination, ideality factor and subgap defect states during reversible light-soaking and irreversible degradation of perovskite solar cells, Energy Environ. Sci. **11,** 151 (2018).

[35] J.-P. Correa-Baena, S.-H. Turren-Cruz, W. Tress, A. Hagfeldt, C. Aranda, L. Shooshtari, J. Bisquert, and A. Guerrero, Changes from bulk to surface recombination mechanisms between pristine and cycled perovskite solar cells, ACS Energy Lett. **2,** 681 (2017).

[36] D. Kiermasch, A. Baumann, M. Fischer, V. Dyakonov, and K. Tvingstedt, Revisiting lifetimes from transient electrical characterization of thin film solar cells; a capacitive concern evaluated for silicon, organic and perovskite devices, Energy Environ. Sci. **11,** 629 (2018).

[37] A. Pockett, G. E. Eperon, T. Peltola, H. J. Snaith, A. Walker, L. M. Peter, and P. J. Cameron, Characterization of planar lead halide perovskite solar cells by impedance spectroscopy, open-circuit photovoltage decay, and intensity-modulated photovoltage/photocurrent spectroscopy, J. Phys. Chem. C **119,** 3456 (2015).

[38] N. Courtier, Interpreting Ideality Factors for Planar Perovskite Solar Cells: Ectypal Diode Theory for Steady-State Operation, Phys. Rev. Appl. **14,** 024031 (2020).

[39] M. Stolterfoht, C. M. Wolff, J. A. Márquez, S. Zhang, C. J. Hages, D. Rothhardt, S. Albrecht, P. L. Burn, P. Meredith, T. Unold, and Dieter Neher, Visualization and suppression

of interfacial recombination for high-efficiency large-area pin perovskite solar cells, Nat. Energy **3,** 847 (2018).

[40] M. Stolterfoht, P. Caprioglio, C. M. Wolff, J. A. Márquez, J. Nordmann, S. Zhang, D. Rothhardt, U. Hörmann, Y. Amir, A. Redinger, Lukas Kegelmann, Fengshuo Zu, Steve Albrecht, Norbert Koch, Thomas Kirchartz, Michael Saliba, Thomas Unold, and Dieter Neher, The impact of energy alignment and interfacial recombination on the internal and external open-circuit voltage of perovskite solar cells, Energy Environ. Sci. **12,** 2778 (2019).

[41] N. E. Courtier, J. M. Cave, J. M. Foster, A. B. Walker, and G. Richardson, How transport layer properties affect perovskite solar cell performance: Insights from a coupled charge transport/ion migration model, Energy Environ. Sci. **12,** 396 (2019).

[42] N. E. Courtier, J. M. Foster, S. O'Kane, A. B. Walker, and G. Richardson, Systematic derivation of a surface polarisation model for planar perovskite solar cells, Eur. J. Appl. Math. **30,** 427 (2019).

[43] P. Calado, A. M. Telford, D. Bryant, X. Li, J. Nelson, B. C. O'Regan, and P. R. Barnes, Evidence for ion migration in hybrid perovskite solar cells with minimal hysteresis, Nat. Commun. **7,** 1 (2016).

[44] P. Calado, I. Gelmetti, B. Hilton, M. Azzouzi, J. Nelson, and P. R. Barnes, Driftfusion: An open source code for simulating ordered semiconductor devices with mixed ionic-electronic conducting materials in one dimension, J. Comp. Electron. **21,** 960 (2022).

[45] M. T. Neukom, S. Züfle, E. Knapp, M. Makha, R. Hany, and B. Ruhstaller, Why perovskite solar cells with high efficiency show small IV-curve hysteresis, Solar Energy Mater. Solar Cells **169,** 159 (2017).

[46] G. Richardson, S. E. O'Kane, R. G. Niemann, T. A. Peltola, J. M. Foster, P. J. Cameron, and A. B. Walker, Can slow-moving ions explain hysteresis in the current–voltage curves of perovskite solar cells?, Energy Environ. Sci. **9,** 1476 (2016).

[47] In Ref. [41] the work functions are not explicitly stated but are related to the quantities E_{f_E} and E_{f_H}, which appear there, via $W_E = -E_{f_E}$ and $W_H = -E_{f_H}$.

[48] C. Eames, J. M. Frost, P. R. Barnes, B. C. O'regan, A. Walsh, and M. S. Islam, Ionic transport in hybrid lead iodide perovskite solar cells, Nat. Commun. **6,** 7497 (2015).

[49] A. Senocrate, I. Moudrakovski, G. Y. Kim, T.-Y. Yang, G. Gregori, M. Grätzel, and J. Maier, The nature of ion conduction in methylammonium lead iodide: A multimethod approach, Angew. Chem. **56,** 7755 (2017).

[50] T.-Y. Yang, G. Gregori, N. Pellet, M. Grätzel, and J. Maier, The significance of ion conduction in a hybrid organic–inorganic lead-iodide-based perovskite photosensitizer, Angew. Chem. **127,** 8016 (2015).

[51] K. Domanski, B. Roose, T. Matsui, M. Saliba, S.-H. Turren-Cruz, J.-P. Correa-Baena, C. Roldán Carmona, G. Richardson, J. M. Foster, F. De Angelis, J. M. Ball, A. Petrozza, N. Mine, M. K. Nazeeruddin, W. Tress, M. Grätzel, U. Steiner, A. Hagfeldt, and A. Abate, Migration of cations induces reversible performance losses over day/night cycling in perovskite solar cells, Energy Environ. Sci. **10,** 604 (2017).

[52] A. Guerrero, E. J. Juarez-Perez, J. Bisquert, I. Mora-Sero, and G. Garcia-Belmonte, Electrical field profile and doping in planar lead halide perovskite solar cells, Appl. Phys. Lett. **105,** 133902 (2014).

[53] L. A. Frolova, N. N. Dremova, and P. A. Troshin, The chemical origin of the p-type and n-type doping effects in the hybrid methylammonium–lead iodide (MAPbI$_3$) perovskite solar cells, ChemComm **51,** 14917 (2015).

[54] O. E. Semonin, G. A. Elbaz, D. B. Straus, T. D. Hull, D. W. Paley, A. M. Van der Zande, J. C. Hone, I. Kymissis, C. R. Kagan, X. Roy, and Jonathan S. Owen, Limits of carrier diffusion in *n*-type and *p*-type CH$_3$NH$_3$PbI$_3$ perovskite single crystals, J. Phys. Chem. Lett. **7,** 3510 (2016).

[55] MATLAB, Matlab version: 9.8.0.1323502 (r2020a) (2020).

[56] H.-S. Kim, I. Mora-Sero, V. Gonzalez-Pedro, F. Fabregat-Santiago, E. J. Juarez-Perez, N.-G. Park, and J. Bisquert, Mechanism of carrier accumulation in perovskite thin-absorber solar cells, Nat. Commun. **4,** 2242 (2013).

[57] M. Bag, L. A. Renna, R. Y. Adhikari, S. Karak, F. Liu, P. M. Lahti, T. P. Russell, M. T. Tuominen, and D. Venkataraman, Kinetics of ion transport in perovskite active layers and its implications for active layer stability, J. Am. Chem. Soc. **137,** 13130 (2015).

[58] P. Löper, M. Stuckelberger, B. Niesen, J. Werner, M. Filipič, S.-J. Moon, J.-H. Yum, M. Topič, S. W. De, and C. Ballif, Complex refractive index spectra of CH$_3$NH$_3$PbI$_3$ perovskite thin films determined by spectroscopic ellipsometry and spectrophotometry., J. Phys. Chem. Lett. **6,** 66 (2015).

[59] F. Brivio, K. T. Butler, A. Walsh, and M. Van Schilfgaarde, Relativistic quasiparticle self-consistent electronic structure of hybrid halide perovskite photovoltaic absorbers, Phys. Rev. B **89,** 155204 (2014).

[60] P. Schulz, E. Edri, S. Kirmayer, G. Hodes, D. Cahen, and A. Kahn, Interface energetics in organo-metal halide perovskite-based photovoltaic cells, Energy Environ. Sci. **7,** 1377 (2014).

[61] C. C. Stoumpos, C. D. Malliakas, and M. G. Kanatzidis, Semiconducting tin and lead iodide perovskites with organic cations: Phase transitions, high mobilities, and near-infrared photoluminescent properties, Inorg. Chem. **52,** 9019 (2013).

[62] A. Walsh, D. O. Scanlon, S. Chen, X. Gong, and S.-H. Wei, Self-regulation mechanism for charged point defects in hybrid halide perovskites, Angew. Chem. **54,** 1791 (2015).

[63] J.-i. Fujisawa, T. Eda, and M. Hanaya, Comparative study of conduction-band and valence-band edges of TiO$_2$, SrTiO$_3$, and BaTiO$_3$ by ionization potential measurements, Chem. Phys. Lett. **685,** 23 (2017).

[64] See Supplemental Material at http://link.aps.org/supplemental/10.1103/PhysRevApplied.19.014061 for details of the analytic model derivation, additional figures, and additional information.

[65] N. Courtier, J. Cave, A. Walker, G. Richardson, and J. Foster, Ionmonger: A free and fast planar perovskite solar cell simulator with coupled ion vacancy and charge carrier dynamics, J. Comput. Electron. **18,** 1435 (2019).

[66] L. Bertoluzzi, C. C. Boyd, N. Rolston, J. Xu, R. Prasanna, B. C. O'Regan, and M. D. McGehee, Mobile ion concentration measurement and open-access band diagram simulation platform for halide perovskite solar cells, Joule **4,** 109 (2020).

[67] D. Meggiolaro, E. Mosconi, and F. De Angelis, Formation of surface defects dominates ion migration in lead-halide perovskites, ACS Energy Lett. **4,** 779 (2019).

[68] A. Castro-Chong, A. J. Riquelme, T. Aernouts, L. J. Bennett, G. Richardson, G. Oskam, and J. A. Anta, Illumination intensity dependence of the recombination mechanism in mixed perovskite solar cells, ChemPlusChem **86,** 1347 (2021).

[69] V. Gonzalez-Pedro, E. J. Juarez-Perez, W.-S. Arsyad, E. M. Barea, F. Fabregat-Santiago, I. Mora-Sero, and J. Bisquert, General working principles of CH$_3$NH$_3$PbX$_3$ perovskite solar cells, Nano Lett. **14,** 888 (2014).

[70] L. Contreras-Bernal, M. Salado, A. Todinova, L. Calio, S. Ahmad, J. Idígoras, and J. A. Anta, Origin and whereabouts of recombination in perovskite solar cells, J. Phys. Chem. C **121,** 9705 (2017).

[71] O. Almora, C. Aranda, E. Mas-Marzá, and G. Garcia-Belmonte, On Mott-Schottky analysis interpretation of capacitance measurements in organometal perovskite solar cells, Appl. Phys. Lett. **109,** 173903 (2016).

[72] I. Zarazua, G. Han, P. P. Boix, S. Mhaisalkar, F. Fabregat-Santiago, I. Mora-Seró, J. Bisquert, and G. Garcia-Belmonte, Surface recombination and collection efficiency in perovskite solar cells from impedance analysis, J. Phys. Chem. Lett. **7,** 5105 (2016).

[73] A. Todinova, L. Contreras-Bernal, M. Salado, S. Ahmad, N. Morillo, J. Idígoras, and J. A. Anta, Towards a universal approach for the analysis of impedance spectra of perovskite solar cells: Equivalent circuits and empirical analysis, ChemElectroChem **4,** 2891 (2017).

[74] G. Paasch and S. Scheinert, Charge carrier density of organics with Gaussian density of states: Analytical approximation for the Gauss–Fermi integral, J. Appl. Phys. **107,** 104501 (2010).

[75] Y. Vaynzof, Y. Preezant, and N. Tessler, Current voltage relation of amorphous materials based *pn* diodes–the effect of degeneracy in organic polymers/molecules, J. Appl. Phys. **106,** 084503 (2009).